Allosteric degraders induce CRL5^{ASB8} mediated degradation of XPO1

Casey E. Wing[1,2], Ho Yee Joyce Fung[1,2,3], Tolga Cagatay[1,2,4], Bert Kwanten[5], Ashley B. Niesman[2,3], Mehdi Gharghabi[6], Brecht Permentier[5], Binita Shakya[2,7], Sharon Shacham[8], Yosef Landesman[8,9], Rosa Lapalombella*[6], Dirk Daelemans*[5] and Yuh Min Chook*[2]

[1] Co-1st authors

[2] Department of Pharmacology, University of Texas Southwestern Medical Center, Dallas, United States, 75390

[3] Department of Biophysics, University of Texas Southwestern Medical Center, Dallas, United States, 75390

[4] Department of Cell Biology, University of Texas Southwestern Medical Center, Dallas, United States, 75390

[5] KU Leuven Department of Microbiology, Immunology and Transplantation, Laboratory of Virology and Chemotherapy, Rega Institute for Medical Research, 3000 Leuven, Belgium

[6] Division of Hematology, Department of Internal Medicine, The Ohio State University, 460 OSUCCC, 410 West 12th Avenue, Columbus, United States, 43210

[7] Department of Clinical, Diagnostic & Therapeutic Sciences, College of Allied Health Professions, University of Nebraska Medical Center, Omaha, United States, 68198

[8] Karyopharm Therapeutics Inc., 85 Wells Avenue, Suite 210, Newton, United States, 02459

[9] Nexgen Biopharma Solutions Inc., 260 Tappan Street, Brookline, United States, 02445

*For correspondence: YuhMin.Chook@utsouthwestern.edu, Dirk.Daelemans@kuleuven.be, Rosa.Lapalombella@osumc.edu

Lead contact: YuhMin.Chook@utsouthwestern.edu

Summary

The nuclear export receptor Exportin 1 (XPO1/CRM1) is often overexpressed in cancer cells resulting in aberrant localization of many cancer-related protein cargoes[1,2]. The XPO1 inhibitor and cancer drug selinexor (KPT-330), and its analog KPT-185, block XPO1-cargo binding thereby restoring cargo localization[2-7]. Selinexor binding induces cullin-RING E3 ubiquitin ligase (CRL) substrate receptor ASB8-mediated XPO1 degradation[7]. Here we reveal the mechanism of inhibitor-XPO1 engagement by $CRL5^{ASB8}$. Cryogenic electron microscopy (cryo-EM) structures show ASB8 binding to a large surface of selinexor/KPT-185-XPO1 that includes a three-dimensional degron unique to the drug-bound exportin. The structure explains weak XPO1-ASB8 binding in the absence of selinexor/KPT-185 that is unproductive for proteasomal degradation, and the substantial affinity increase upon selinexor/KPT-185 conjugation, which results in $CRL5^{ASB8}$-mediated XPO1 ubiquitination. In contrast to previously characterized small molecule degraders, which all act as molecular glues[8-10], selinexor/KPT-185 binds extensively to XPO1 but hardly contacts ASB8. Instead, selinexor/KPT-185 binds XPO1 and stabilizes a unique conformation of the NES/inhibitor-binding groove that binds ASB8. Selinexor/KPT-185 is an allosteric degrader. We have explained how drug-induced protein degradation is mediated by a CRL5 system through an allosteric rather than a molecular glue mechanism, expanding the modes of targeted protein degradation beyond the well-known molecular glues of CRL4.

Main text

Exportin 1 (XPO1), also known as chromosome region maintenance 1 (CRM1), transports hundreds to thousands of broadly functioning classical nuclear export signal (cNES) containing proteins and RNAs from the nucleus[1]. XPO1 cargoes include tumor suppressor proteins, cell cycle regulators, and apoptotic factors and oncogene mRNAs[1]. XPO1 is overexpressed in many cancers and is associated with poor prognosis due to nuclear depletion of many tumor suppressor and pro-apoptosis cargoes, and increased cytoplasmic accumulation of many oncogene mRNAs. Aberrant localization of XPO1 cargoes may result in evasion of apoptosis and/or stimulate oncogenesis, conferring survival advantage to cancer cells (reviewed in [2]).

XPO1 inhibition as anti-cancer strategy included the unsuccessful Phase 1 clinical trial of the toxic lactone polyketide natural product inhibitor Leptomycin B (LMB) [2,11-13]. Smaller synthetic N-azolylacrylate XPO1 inhibitors termed KPT-SINE compounds (KPT, Karyopharm Therapeutics Inc.; SINE, Selective Inhibitor of Nuclear Export) effectively target a variety of cancers and one KPT-SINE, selinexor/XPOVIO® (KPT-330), has been approved by the FDA for treatment of multiple myeloma and diffuse large B-cell lymphoma[2,3,13-22]. KPT-SINE compounds (SINE) and LMB have α,β-unsaturated groups that undergo Michael addition reaction to covalently conjugate Cys528 in the XPO1 NES-binding groove, directly blocking XPO1-NES/cargo interactions and nuclear export[17,22-28].

In addition to inhibiting nuclear export, many SINE compounds also cause XPO1 degradation[4-6,17], while LMB does not have degrader activity[29]. The chemically distinct covalent XPO1 inhibitor felezonexor (CBS9106/SL-801, Stemline Therapeutics) also

causes XPO1 degradation that was suggested to be mediated by Cullin-RING E3 ubiquitin ligases (CRLs) [29,30]. We recently reported the discovery through CRISPR loss-of-function screens with selinexor that the E3 ligase substrate receptor Ankyrin and SOCS box containing protein 8 (ASB8) mediates selinexor-induced XPO1 degradation[7].

Selinexor-induced XPO1 degradation is mediated by cullin E3 ring ligase

Even though covalent XPO1 inhibitors such as selinexor, its analogs KPT-185 and KPT-8602 (eltanexor) as well as the distinct inhibitor felezonexor all cause dose- and time-dependent reduction of XPO1 levels in cells[4,5,17,19,29,31,32], pulse-chase studies in the absence of inhibitor show that endogenous XPO1 in HT1080 cells is very long-lived (**Figure 1a,b**). XPO1 protein levels are stable even after 48 hours. Treating cells with KPT-185 or selinexor (used interchangeably in this study) gradually decreased XPO1 protein levels, which recovered following inhibitor removal (**Extended Data Figure 1a,b**). Proteasome inhibitor MG132 (like bortezomib treatment as shown by others[4,33]) and neddylation inhibitor MLN4924 prevented SINE-induced XPO1 degradation, suggesting involvement of the proteasome and a CRL, respectively (**Extended Data Figure 1c**). The higher molecular weight XPO1 protein band that appeared after selinexor/MG132 treatment, but not with MLN4924 treatment, is likely ubiquitinated XPO1, as shown by co-transfection of HA-ubiquitin and FLAG-XPO1 and *in vitro* experiments with vOTU deubiquitinase in **Figure 1c,d**. The XPO1 C528 residue conjugates all known covalent XPO1 inhibitors and confers resistance to the inhibitors[17,22-28,34]. Mutating C528 of XPO1 to a threonine prevents SINE conjugation and SINE-induced degradation of the XPO1 mutant in cells (**Extended Data Figure 1d**).

All the above results show that SINE-conjugated XPO1 (SINE-XPO1) is targeted by CRL for degradation by the proteasome, in agreement with our previous results[7].

SINE-XPO1 binds CRL5^{ASB8} for degradation

We recently reported that overexpression of CRL substrate receptor ASB8 stimulates selinexor-induced XPO1 degradation, whereas knockout inhibited degradation[7]. We therefore examined selinexor-induced XPO1 degradation and ASB8 level in primary samples from patients with chronic lymphocytic leukemia (CLL) and in the HG3 CLL cell line (**Figure 1e**). Selinexor induces degradation of XPO1 in HG3 cells in a time- and dose-dependent manner. Selinexor also induces degradation of XPO1 in primary CLL cells. Interestingly, the level of ASB8 increased upon selinexor treatment.

ASB8 is a member of the human ANKyrin repeat and SOCS box containing protein (ASB) family, and SINE-XPO1 is its only substrate reported thus far. ASB8 contains an N-terminal helix (N^{helix}), seven ANKyrin repeats (ANK1-7, each with antiparallel helices α1, α2) and a C-terminal SOCS box (AF-Q9H765-F1, **Figure 1f**) [35]. We hypothesize that, like other ASB proteins, the ASB8 SOCS box binds the heterodimeric Elongin B-Elongin C (ELOB/C) CRL adaptor, which in turn binds Cullin 5 (CUL5) (**Figure 1f**) [35,36]. NEDDylation of CUL5 is expected to activate the E2 enzyme and RING-box protein 1/2 (RBX1/2) bound CRL5^{ASB8} to ubiquitinate SINE-XPO1 for degradation by the proteasome (**Figure 1f**) [37,38].

Other than ASB8, other CRL5^{ASB8} components had not been examined for involvement in SINE-induced XPO1 degradation. siRNA knockdowns of ELOB, CUL5 and RBX1/2 all decreased SINE-XPO1 degradation, further supporting CRL5^{ASB8} involvement (**Figure 1g**, **Extended Data Figure 1e**). Although we could co-

immunoprecipitate XPO1 with ASB8 in a selinexor dose dependent manner from cellular extracts[7], it was unclear if ASB8 binds directly to selinexor-XPO1. We examined direct interaction of SINE-XPO1 with a recombinant ASB8•ELOB/C complex. Immobilized GST-ASB8•ELOB/C pulled down SINE-XPO1 but not LMB-XPO1 nor unliganded XPO1, showing direct and specific ASB8 binding to SINE-XPO1 (**Figure 1h**, **Extended Data Figure 2a**).

Cryo-EM structures of SINE-XPO1 bound to the ASB8•ELOB/C complex

We next assembled complexes of selinexor-XPO1 and KPT-185-XPO1 bound to the ELOB/C-bound $ASB8^{\Delta N16}$ (N^{helix} removal decreased aggregation) for cryogenic electron microscopy (cryo-EM) structure determination. We solved the Ran^{GTP}-bound selinexor-XPO1•ASB8•ELOB/C structure to 3.3 Å resolution and the KPT-185-XPO1•ASB8•ELOB/C structure to 3.4 Å resolution (**Figure 2a,b**, **Extended Data Table 1** and **Figure 3**). We also solved cryo-EM structures of unliganded and selinexor-bound XPO1 at 2.9 Å and 3.4 Å resolution, respectively, for comparison even though the structures are very similar previously published crystal structures (PDB: 3VYC, 4FGV and 7L5E) [27,39,40] (**Extended Data Table 1** and **Figure 4 and 5**).

The cryo-EM maps for Ran^{GTP}•selinexor-XPO1•ASB8•ELOB/C and KPT-185-XPO1•ASB8•ELOB/C are very similar except that Ran^{GTP}-binding in the former ordered the N-terminal HEAT repeats of XPO1 while the same region (HEAT repeats h1-h4 and helices h5A or h6A) of the latter is dynamic and not resolved in the map (**Figure 2a,b**). ASB8 ANK1 repeat is not resolved in neither map. First, we built the KPT-185-XPO1•ASB8•ELOB/C structure using the AlphaFold model of ASB8, the ASB9-bound ELOB/C structure (PDB: 6V9H) [36] and the cryo-EM structure of selinexor-XPO1 from

this study, (**Figure 2b**). Next, we built the Ran^{GTP}•selinexor-XPO1•ASB8•ELOB/C structure using ASB8•ELOB/C from the KPT-185-XPO1•ASB8•ELOB/C structure, and XPO1 and Ran^{GTP} from previous crystal structures (6TVO, 3M1I) [41] (**Figure 2a**).

ASB8•ELOB/C binds similarly to selinexor-XPO1 and KPT-185-XPO1 (**Figure 2a,b**). The concave surface of the ASB8 ANK domain solenoid (ANK2-7) abuts the convex surface of XPO1 at HEAT repeats h10-h12, which includes the inhibitor-bound groove, while the ASB8 C-terminal SOCS box packs against the convex surface of its ANK5 and ANK6 repeats like in ASB9[36] (**Figure 2a-c**, **Extended Data Figure 6a**). The ASB8 SOCS box binds the ELOB/C heterodimer the same way that the ASB9 SOCS binds ELOB/C, and alignment of the ASB8-bound CRL adaptor allowed overlay of the RBX1 bound NEDD8-CUL5 (**Extended Data Figure 6b**) [36,42-44].

KPT-185 and selinexor bind XPO1 similarly regardless of whether ASB8•ELOB/C is bound, except the pyrazinylpropenehydrazide arm of selinexor is more flexible (**Extended Data Figure 3c and 4f**). The two structures are very similar at the regions where selinexor-XPO1 and KPT-185-XPO1 bind ASB8•ELOB/C, with Cα r.m.s.d. values of 0.7 Å for XPO1 central HEAT repeats h10-12 and 0.5 Å for ASB8•ELOB/C. The N- and C-terminal HEAT repeats of the two XPO1 solenoids differ slightly (Cα r.m.s.d. 1.9 Å) because of the Ran^{GTP} that is bound to the selinexor-XPO1•ASB8•ELOB/C complex (**Figure 2a,b**).

Interactions between ASB8 and the selinexor/KPT-185-bound XPO1

Here, we focus on KPT-185-XPO1•ASB8•ELOB/C structure for interaction analysis because of the map has better side chain features at the XPO1-ASB8 interface

(Figure **3a,b**). The same interface in the Ran^{GTP}•selinexor-XPO1•ASB8•ELOB/C structure is very similar (**Extended Data Figure 7**).

ASB8 covers 993 Å^2 of XPO1 and ASB8-XPO1 contacts are concentrated at two ends of the interface that spans XPO1 h10-h12 (**Figure 2c**). At one end, XPO1 h10 and h11 (h10/11) make many contacts with ANK repeats 3 and 4 (ANK3/4) (**Figure 3a**). At the other end, the KPT-185-bound XPO1 groove at HEAT repeats h11 and h12 (h11/12) contacts the ANK repeats 6 and 7 (ANK6/7) (**Figure 3b**). Most of the KPT-185 molecule bound in the XPO1 groove is far from ASB8 except for the methoxy group which makes a single contact with the ASB8 R197 side chain (**Figure 3c**). Similarly, most of the conjugated selinexor is also far from ASB8. One of its trifluoromethyl (TFM) group also makes a single contact with ASB8 R197 (**Figure 3d**).

The interface between XPO1 h10/11 and the α1 helices of ASB8 ANK3/4 involves a variety of polar, electrostatic, and hydrophobic interactions (**Figure 3a**). We mutated six XPO1 residues here (E478A, H481A, V484G, N485G, T487G, and D523G; named XPO1$^{h10/11}$ mutant), which substantially decreased KPT-185 dependent binding to GST-ASB8•ELOB/C (**Figure 3e**). Mutation of the ASB8 contact residues (R87A, E95A, K96A, W124A, and K128A; named ASB8$^{ANK3/4}$ mutant) similarly decreased binding to KPT-185-XPO1.

At the other end of the interface, ASB8 ANK6/7 contacts XPO1 h11/12, which is the inhibitor/NES-binding groove (**Figure 3b**). The XPO1 groove is lined with five hydrophobic pockets P0-4 (**Figure 2c**). SINE inhibitors bind across the P2-P4 pockets, wedging the entire groove open such that pockets P0 and P1 unoccupied and exposed[17,23-27]. In the KPT-185-XPO1•ASB8•ELOB/C structure, XPO1 pockets P0 and

P1 bind ASB8 residues ^{196}VRGL^{199} of the last helix turn of the ANK6 α1 helix and the loop that follows (**Figure 3b**). The ASB8 L199 side chain binds the XPO1 P1 pocket while ASB8 ^{196}VRG^{198} come very close to XPO1. Here, the main chain carbonyls of ASB8 ^{196}VRG^{198} make multiple contacts with the main and side chains of the XPO1 h12A helix (**Figure 3c**). Nearby, ASB8 ANK7 residues R232 and D233 make electrostatic interactions with XPO1 K560 and E571, respectively (**Figure 3b**); the latter an oncogenic mutation site E571[45-48]. Mutations of XPO1 V518 and F561 of the ASB8-binding site to Asp and His, respectively (named XPO1^{EH}), altered the hydrophobic P0 and P1 pockets to a charged surface and substantially decreased ASB8 binding (**Figure 3f**). Mutations of ASB8 R197G/L199G to destabilize the last helical turn of the ANK6 α1 helix or R197G/L199R to generate steric clash with the XPO1 P1 pocket also decreased ASB8-XPO1 interactions.

All the interface mutations above resulted in a reduction of selinexor-induced XPO1 degradation. Transient overexpression of ASB8 and XPO1 wild type (WT) in combination with selinexor treatment typically results in extensive XPO1 degradation (**Figure 4a**). However, constructs carrying mutations at the XPO1-ASB8 interface lose this ability (**Figure 4a-b**). Moreover, while overexpression of ASB8 WT sensitizes cells to selinexor because of severe XPO1 depletion, this effect is absent in cells expressing any one of the mutant ASB8 proteins (**Figure 4c**). Collectively, the structural, biochemical, and cellular results above reveal the importance of interactions between inhibitor-bound XPO1 h10/11 with ASB8 ANK3/4 and between the P0 and P1 pockets of the KPT-185-bound XPO1 groove with ASB8 ANK6 residues ^{196}VRGL^{199} for engagement of inhibitor-XPO1 by CRL5^{ASB8} for XPO1 degradation.

The degron specific to selinexor/KPT-185-bound XPO1

The selinexor/KPT-185-XPO1 degron, defined as the XPO1 interface with ASB8, spans the convex surface HEAT repeats h10-h12 (**Figure 2a-c**). Within the degron, XPO1 repeats h10 and h11 adopt the same conformation in many different XPO1 structures; Cα r.m.s.d. of residues 469-552 is 0.6 - 1.0 Å when comparing unliganded, NES-, inhibitor-, RanBP3- and nucleoporin-bound structures (**Figure 5a**) [24,49-51]. The XPO1 side chains that contact ASB8 ANK3/4 are all solvent-accessible in the different structures. The h10/11 degron is not unique to selinexor/KPT-185-bound XPO1.

In contrast, the degron at the XPO1 groove (h11 and h12), termed the groove degron, is very different depending on the bound ligand (**Figure 5a,b**). The groove is closed in unliganded XPO1 and the ASB8-binding site is thus inaccessible (**Figure 5b**). NES peptides with diverse sequences adopt diverse conformations when they bind the XPO1 groove, but all characterized NESs bind minimally across the P1-P3 pockets (**Figure 5c**, **Extended Data Figure 8**) [52,53]. XPO1-NES binding is thus incompatible with ASB8-binding. LMB occupies the entire XPO1 groove leaving no room for ASB8 to bind, in agreement with LMB not inducing XPO1 degradation (**Figure 5d**) [24,29]. Smaller SINE compounds like selinexor and KPT-185 only occupy P2-P4[17,23,25-27], leaving the P0 and P1 pockets exposed for ASB8 to bind (**Figure 5e**). The crystal structure of the groove degron mutant $XPO1^{EH}$ bound to KPT-185 show a polar/charged groove with shallower pockets P0 and P1 that is not compatible with ASB8-binding (**Figures 3e**, **4a**, **5f**, **Extended Data Figure 9a,b** and **Table 2**). The groove degron is unique to selinexor/KPT-185-bound XPO1 and specific for ASB8-binding (**Figure 5b**).

The presence of the nearby conformationally invariant h10/11 degron in all known XPO1 states suggest that the exportin has basal low affinity for ASB8 even in the absence of inhibitors. Indeed, competition binding assays showed that high concentrations of ASB8 can compete with XPO1-NES binding (**Figure 5g**). Similarly, we also observed direct XPO1-ASB8 pull down at high protein concentrations in the absence of inhibitor (**Figure 5h**). We estimate ASB8-XPO1 binding in the absence of inhibitor to be in the low micromolar affinity range, which is too weak for productive ubiquitination and degradation[54].

Other XPO1 inhibitors and CRL5^{ASB8}-mediated XPO1 degradation

The location of the selinexor/KPT-185 induced groove degron at one end the XPO1 groove suggests that larger analog compounds with moieties that extend from the TFM/methoxy groups of selinexor/KPT-185, respectively, should block access to the degron and clash with ASB8 (**Figure 5e**). We solved the 2.4 Å resolution crystal structure of XPO1 conjugated to KPT-396, which has a larger oxypropyne group in place of the TFM of selinexor and tested its ability to induce XPO1 degradation (**Figure 6a,b**, **Extended Data Figure 9c-e** and **Table 2**). The structure places the flexible KPT-396 oxypropyne (no electron density) extending toward solvent where it would clash with the ASB8 R197 side chain, explaining its inability to induce XPO1 degradation.

We also aligned our KPT-185•XPO1•ASB8•ELOB/C structure with those of XPO1 bound to the SINE eltanexor[17] (**Extended Data Figure 11a**) and two non-SINE inhibitors, felezonexor analog S109 and the non-covalent inhibitor NCl-1[55] (**Figure 6c,d**). The aligned S109 and eltanexor compounds do not clash with ASB8, suggesting likely CRL5^{ASB8} mediated XPO1 degradation that is induced by S109/felezonexor or

eltanexor conjugation. We show in **Extended Data Figure 11b** that felezonexor- and eltanexor-XPO1 indeed bind ASB8•ELOB/C. The ability of NCI-1 to cause XPO1 degradation has not been reported[55], but structural alignment shows a clash of its bis(TFM)phenyl group with Arg197 of ASB8, suggesting that NCI-1 may not induce $CRL5^{ASB8}$ mediated XPO1 degradation.

Selinexor and KPT-185 act as allosteric degraders

XPO1-bound selinexor/KPT-185 is far from ASB8 and makes almost no contact with ASB8 (**Figure 3c,d**). Each inhibitor makes only one van der Waals contact with the ASB8 Arg197 side chain. Mutation of ASB8 Arg197 to alanine (ASB8 R197A) did not affect binding to selinexor/KPT-185-XPO1 (**Figure 6e)**, suggesting that the single SINE-ASB8 contact that we observe in the structures (**Figure 3c,d**) is not important for XPO1-ASB8 interaction. Therefore, selinexor and KPT-185 appear to act allosterically (**Figure 6f**).

Selinexor and KPT-185 each conjugate to XPO1 Cys528 at the groove. They make many non-covalent interactions with other groove residues and stabilize the open groove conformation. However, they each occupy only half of the XPO1 groove but keep the remainder of the groove open, exposing the normally buried hydrophobic pockets P0/P1 to create the groove degron for ASB8 to bind. S109 binding to XPO1 also exposes P0/P1, suggesting that S109/felezonexor most likely also act allosterically (**Figure 6c**).

The mechanism of how selinexor/KPT-185 induces recruitment of $CRL5^{ASB8}$ to XPO1 is distinct from those of other small molecule degraders that all seem to act as molecular glues[8,56,57]. Most molecular glue degraders bind E3 Ligase substrate

receptors to create new interfaces that recruit neo-substrates (examples: auxin/jasmonate, thalidomide/lenalidomide/pomalidomide and indisulam/E7820) [9,10,57-61]. Others like the cyclin-dependent kinase inhibitor CR8 glues a CRL adaptor to a neo-substrate receptor, and the BI-3802 degrader glues BCL6 α and β subunits into filaments for ubiquitination by non-CRL E3 ligase SIAH1[62,63].

Molecular glue degraders tend to bind weakly to substrates or E3 substrate receptors alone, binding with high affinity only when both are present[54,60-62]. Selinexor/KPT-185 acts differently as it is covalently conjugated to XPO1 with a half-life of 1-2 days[21] and does not bind ASB8. Selinexor/KPT-185 wedges the XPO1 groove open for ASB8-binding. Selective estrogen receptor downregulator (SERD) compounds were proposed to expose a hydrophobic surface of the estrogen receptor α (ERα), thus suggestive of an allosteric mechanism, but the identity of the E3 ligase and structural evidence for the hypothesized mechanism remain absent[64].

Conclusions

The CUL5 substrate receptor ASB8 binds directly and specifically to KPT-XPO1, allowing the $CRL5^{ASB8}$ complex to ubiquitinate XPO1 for degradation by the proteasome. In the absence of inhibitor, XPO1 binds ASB8 weakly. Covalent conjugation and extensive interactions of selinexor/KPT-185 with XPO1 but not ASB8, results in high affinity XPO1-ASB8 binding through an allosteric mechanism. Selinexor/KPT-185-binding stabilizes a unique open-groove XPO1 conformation that exposes a hydrophobic neo-degron to engage $CRL5^{ASB8}$.

Acknowledgements

We thank the Structural Biology Laboratory and the Cryo-EM Facility at UTSW for cryo-EM data collection (Cancer Prevention & Research Institute of Texas or CPRIT RP220582), and the Advanced Photon Source, operated for the DOE Office of Science by Argonne National Laboratory under Contract No. DE-AC02-06CH11357 for X-ray crystallography data collection. We thank H. Niederstrasser and B. A. Posner of the High-Throughput Screening Core Facility of UTSW (National Institutes of Health (NIH) shared instrumentation grant 1S10OD018005-01 to B.A.P. and the Simmons Cancer Center Support grant - Arteaga 2P30CA142543-11) for siRNA analysis. This work was funded by the National Institute of General Medical Sciences of the NIH under R35GM144137 (Y.M.C.) and the Molecular Biophysics Training Program T32GM131963 (C.E.W.), the National Cancer Institute of the NIH under R01 CA214046 (R.L.), the Welch Foundation grant I-1532 (Y.M.C.), CPRIT grants RP180410, RP150053 and RP170170 (Y.M.C.), support from the Alfred and Mabel Gilman Chair in Molecular Pharmacology (Y.M.C.), Eugene McDermott Scholar in Biomedical Research (Y.M.C.), the FWO (Fonds Wetenschappelijk Onderzoek) grant G0E6517N (D.D), the HHMI International Fellowship (H.Y.J.F.) and the Gilman Special Opportunities Award (H.Y.J.F.). We are grateful to the patients who provided blood for the above studies and to the OSU Comprehensive Cancer Center Leukemia Tissue Bank (supported by NCI P30 CA016058) for sample procurement.

Author Contributions: The project was conceived by Y.M.C with inputs from T.C., H.Y.J.F. and C.E.W.. The manuscript was written by Y.M.C., C.E.W. and H.Y.J.F. with inputs from D.D., B.K. and R.L. Cellular experiments were performed T.G., and biochemical experiments by C.E.W., A.B.N. and B.S.. Cryo-EM and crystal structures

were determined and analyzed by C.E.W. and H.Y.J.F.. Cellular experiments with XPO1 mutants were performed by B.K. and B.P. , with input from D.D.. Cellular experiments with CLL cells were performed by M.G., with input from R.L.. KPT-185, selinexor, KPT-396 and KPT-404 were provided by Karyopharm Therapeutics, with input by Y.L. and S.S.

Competing Interests: Y.M.C. was a consultant and holds equity options in Karyopharm Therapeutics. Y.M.C is also a consultant in Telo Therapeutics. B.K., B.P. and D.D. are employees of KU Leuven, which has a license agreement on KPT-SINE XPO1 inhibitors. Y.L. was an employee of Karyopharm Therapeutics and still retains ownership of company shares. S.S. is a former employee of Karyopharm Therapeutics and holds patents (8999996, 9079865, 9714226, PCT/US12/048319, and I574957) on hydrazide-containing nuclear transport modulators and uses and holding pending patents (PCT/US12/048319, 499/2012, PI20102724, and 2012000928) on hydrazide-containing nuclear transport modulators and uses.

Supplementary Materials

Methods

Extended Data Tables 1 and 2

Extended Data Figures 1 to 11

Figures & legends

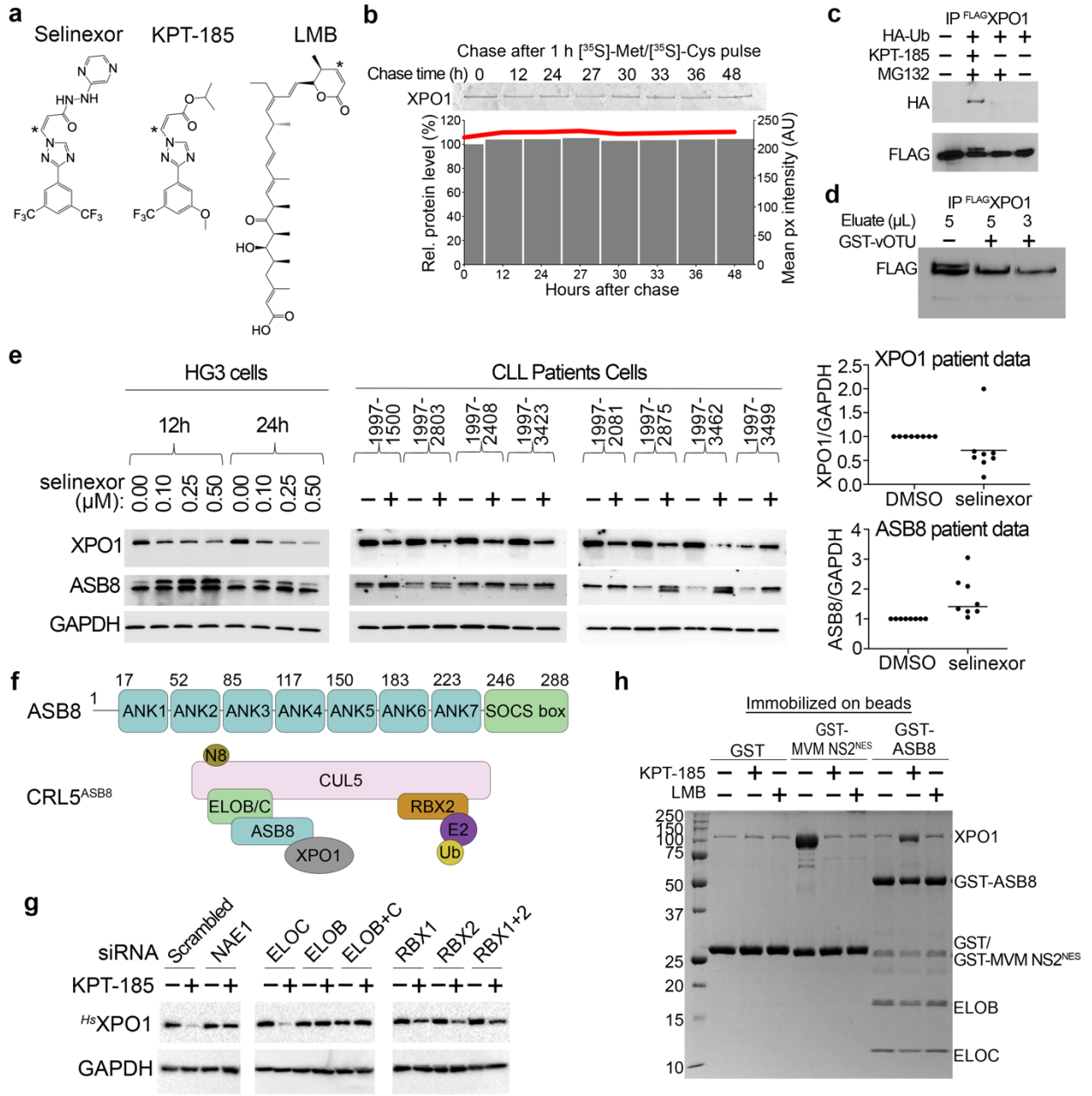

Figure 1. CRL5^{ASB8} binds and degrades selinexor/KPT-185-XPO1.

a, Chemical structures of selinexor, KPT-185, and LMB.

b, Pulse-chase experiment in HT1080 cells, with a 1 h pulse of [^{35}S]-Met/[^{35}S]-Cys and XPO1 IP-ed over 48 h.

c, HEK-293$^{FLAG\text{-}XPO1}$ cells transfected with HA-ubiquitin were treated with DMSO or KPT-185 followed by MG132. ^{FLAG}XPO1 IPed from cell lysates subjected to WB with anti-HA antibody.

d, ^{FLAG}XPO1, IP-ed from HEK-293$^{FLAG\text{-}XPO1}$ cells treated with selinexor and MG132, was treated with GST-vOTU deubiquitinase. WB shows disappearance of the higher molecular weight ^{FLAG}XPO1 band after deubiquitinase treatment.

e, Expression level of XPO1 and ASB8 by WB in HG3 cells or CLL cells from patients treated with DMSO or selinexor. Primary CLL cells were treated at 0.5 μM selinexor for 24h. Quantitation of XPO1 and ASB8 protein levels in CLL patient cells shown on the right. Loading control is GAPDH.

f, Domain organization of ASB8 and schematic of the inhibitor-XPO1•CRL5^{ASB8} complex.

g, XPO1 level in HT1080 cells treated with KPT-185 and siRNAs of CRL5^{ASB8} components. Detection by WB, loading control is GAPDH and positive control is NAE1 siRNA.

h, Pull-down assay of immobilized GST-ASB8•ELOB/C (negative control, immobilized GST) with XPO1 pre-treated with the indicated compounds. Bound proteins are visualized by Coomassie SDS-PAGE shows the bound proteins. Unbound proteins shown in **Extended Data Figure 2a**.

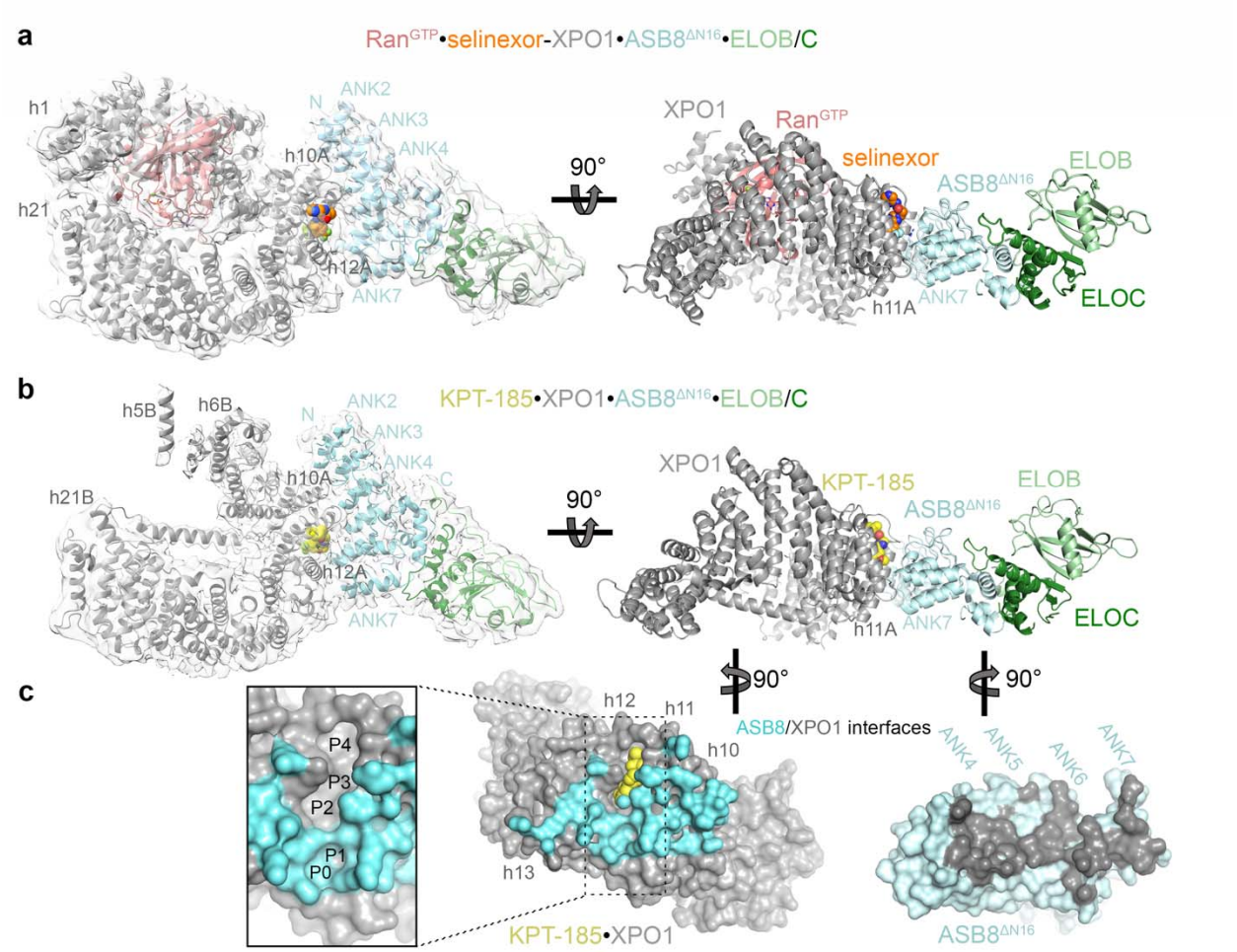

Figure 2. Cryo-EM structures of the Ran^{GTP}•selinexor-XPO1•ASB8•ELOB/C and KPT-185-XPO1•ASB8•ELOB/C complexes.

a, Cryo-EM map and refined structure of Ran^{GTP} (pink)•selinexor (orange spheres)-XPO1 (gray)•ASB8$^{\Delta N16}$ (cyan)•ELOB/C (light/dark green).

b, Cryo-EM map and refined structure of KPT-185 (yellow spheres)-XPO1 (gray)•ASB8$^{\Delta N16}$ (cyan)•ELOB/C (light/dark green).

c, XPO1 and ASB8 surfaces in grey and light cyan, respectively. Butterfly views show the ASB8 interface of XPO1 (cyan) and the XPO1 interface of ASB8 (dark grey). An insert shows the XPO1 groove with KPT-185 removed to reveal the P0-4 hydrophobic pockets.

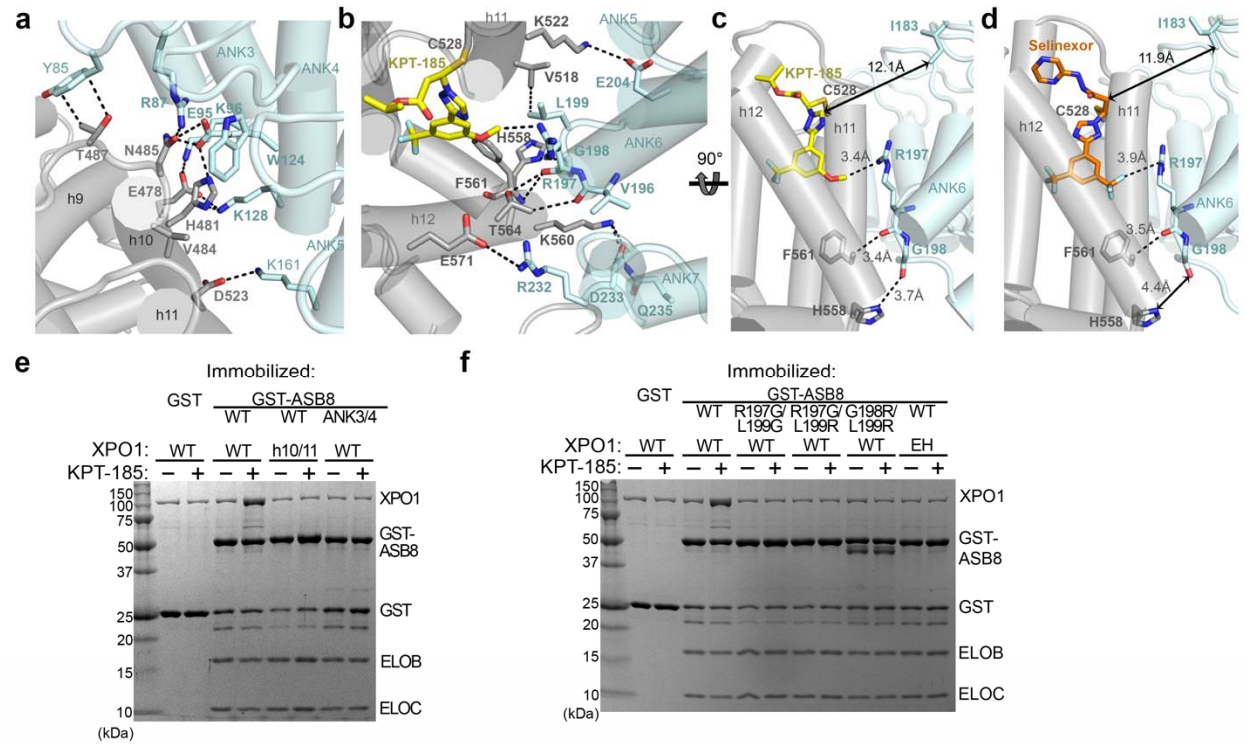

Figure 3. The XPO1-ASB8 interaction interface.

a, The XPO1-ASB8 h10/11-ANK3/4 interface. Dashed lines show contacts <4Å and all XPO1 and ASB8 side chains shown were mutated to generate XPO1$^{h10/11}$ and ASB8$^{ANK3/4}$ mutants, respectively, for experiments in panel **(e)**.

b, The XPO1-ASB8 h11/12-ANK6/7 interface. Left, dashed lines show contacts <4Å.

c-d, Side view of the interfaces in **b** in KPT-185-XPO1•ASB8•ELOB/C (**c**) and Ran^{GTP}•selinexor-XPO1•ASB8•ELOB/C (**d**).

e,f, Pull-down assay of immobilized GST-ASB8•ELOB/C mutants with XPO1 and KPT-185 or DMSO, visualized by Coomassie staining. Mutations target the h10/11-ANK3/4 (**e**) and the h11/12-ANK6/7 interfaces (**f**). Unbound proteins are shown in **Extended Data Figure 2c.**

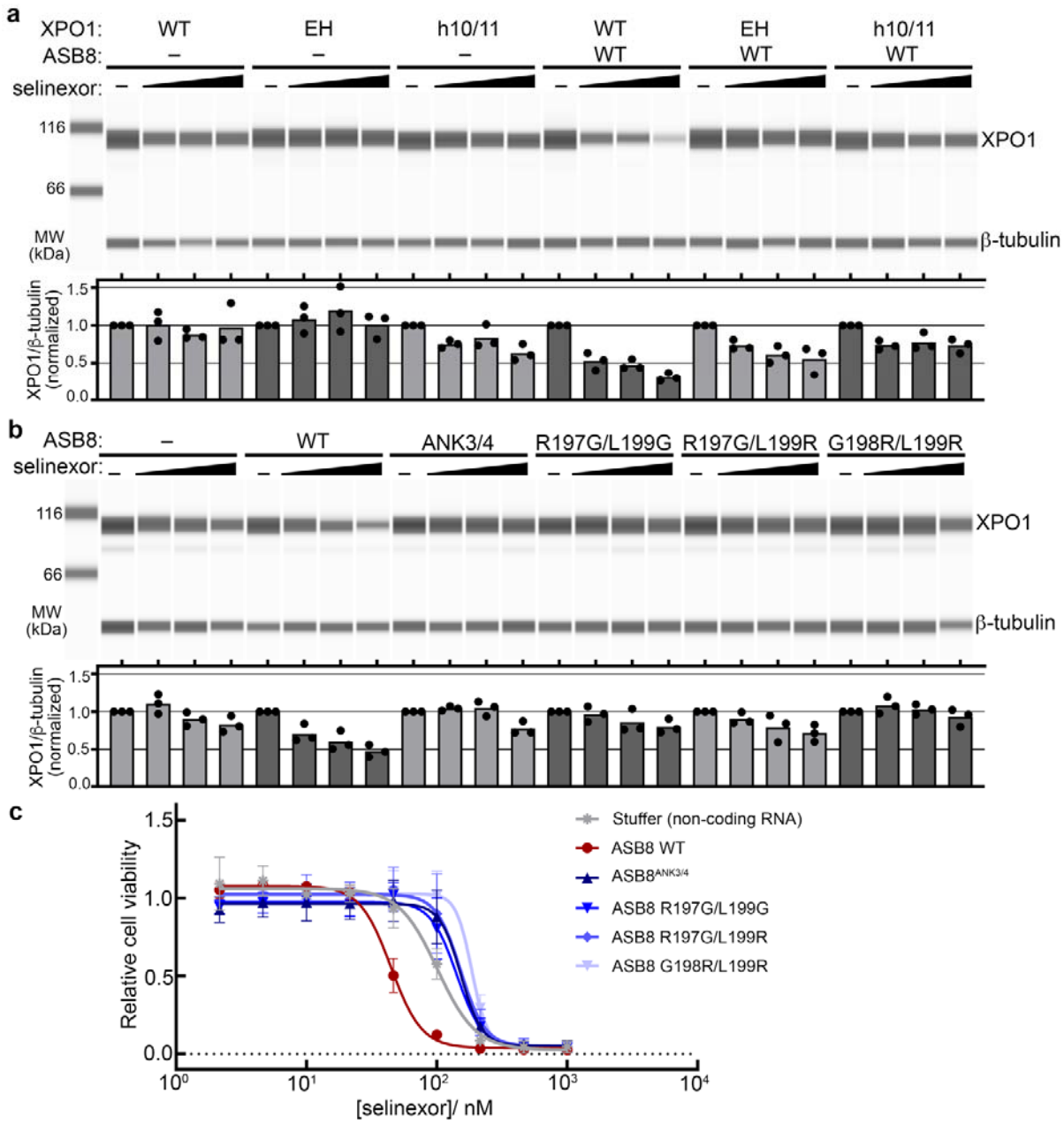

Figure 4. Mutations at the XPO1-ASB8 interface abrogate XPO1 degradation.

a, HEK293T cells were transfected with XPO1 WT, XPO1^{EH} or XPO1$^{h10/11}$ alone or together with ASB8 WT and treated overnight with selinexor. XPO1 degradation was assessed by WB.

b, Transfection with ASB8 WT, ASB8$^{ANK3/4}$ and ASB8 mutants R197G/L199G, R197G/L199R or G198R/L199R followed by overnight treatment with selinexor and WB analysis of XPO1. Representative WB images are shown in **a** and **b** with β-tubulin as a loading control. For densitometric analysis, normalized XPO1/β-tubulin peak area values from three separate experiments were averaged.

c, Cell viability assay on HAP1 cells with stable overexpression of ASB8 WT or one of the ASB8 mutants. Data points were normalized to untreated cells and represent mean ±SD of three separate experiments.

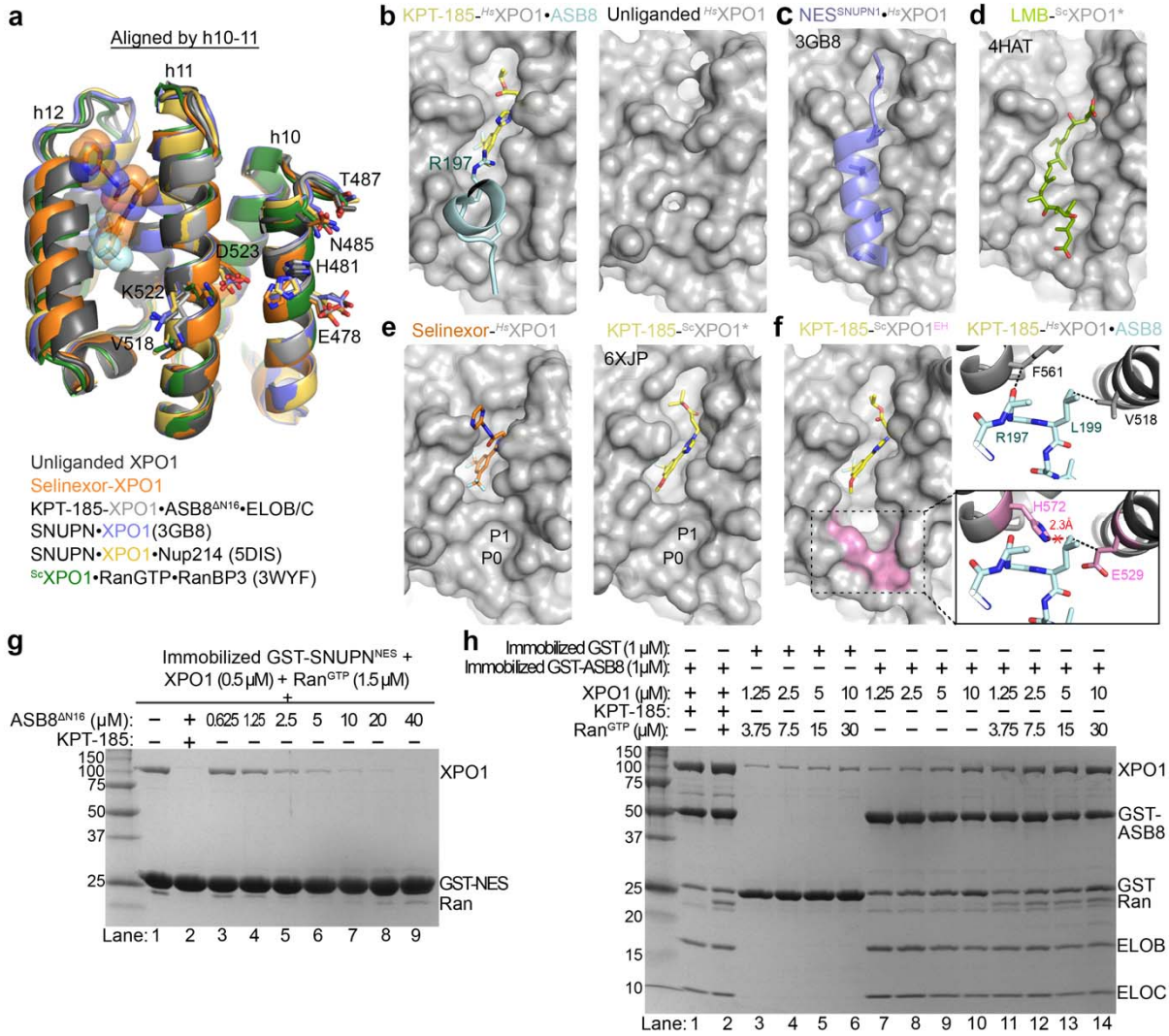

Figure 5. The KPT-185-XPO1 degron.

a, The XPO1 h10-12 of several XPO1 structures, aligned at h10/11 and shown as cartoons. Selinexor is shown as spheres, and h10/11 side chains that contact ASB8 are shown as sticks.

b, The NES/inhibitor-binding grooves of KPT-185•XPO1•ASB8 and the unliganded XPO1.

c-e, The NES^{SNUPN1} (slate) bound XPO1 groove (3GB8) (**c**), the LMB (light green) bound XPO1 groove (4HAT) (**d**), the Selinexor- and KPT-185- bound (6XJP) XPO1 grooves (**e**), all in the same view as **b**.

f, The KPT-185-bound groove of the XPO1EH mutant. An insert shows ASB8 aligned and the likely steric clash. The same view of KPT-185•XPO1•ASB8 is shown above for comparison.

g, Competition pull-down assay of XPO1 binding to immobilized GST-NES (in the presence of Ran^{GTP}), in the absence/presence of $ASB8^{\Delta N16}$•ELOB/C and KPT-185.

h, Pull-down assay to assess direct binding of XPO1 to immobilized GST-ASB8-ELOB/C, in the absence/presence of KPT-185 and Ran^{GTP}. Gels in **g** and **h** were visualized by Coomassie staining with unbound proteins shown in **Extended Data Figure 10a,b**.

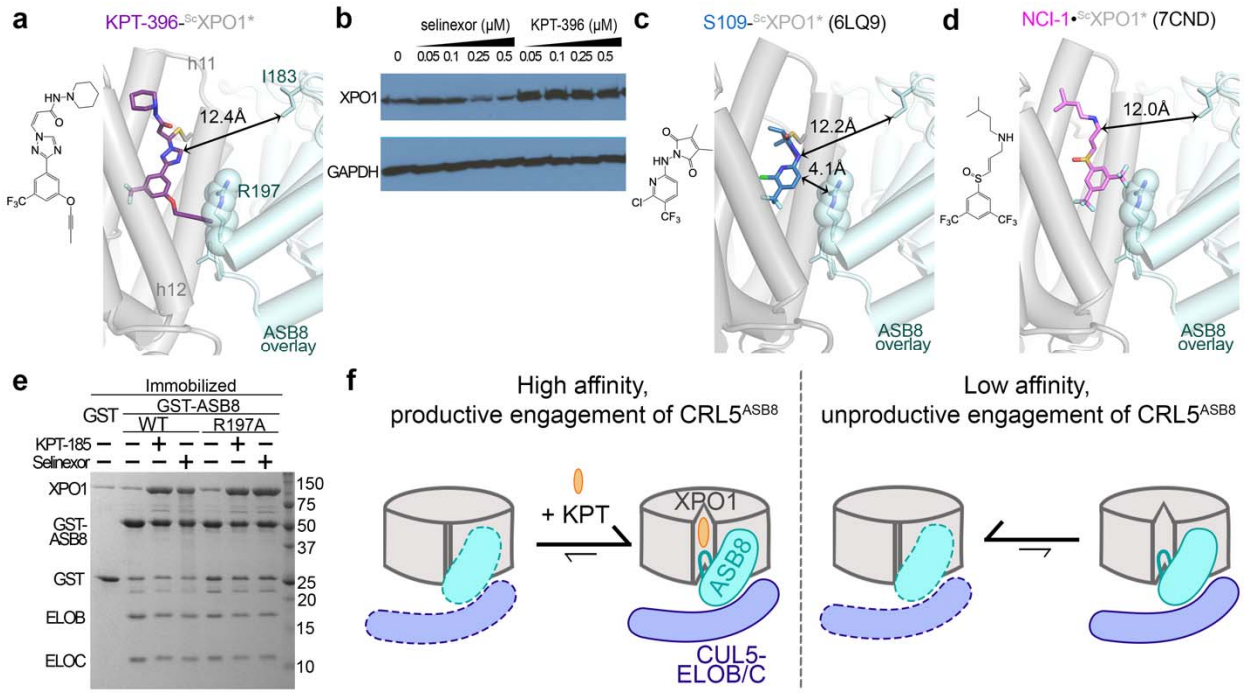

Figure 6. The ASB8-binding site in other inhibitor-bound XPO1 structures and the mechanism of selinexor/KPT-185 as allosteric degrader.

a, The chemical structure of KPT-396, and the KPT-396-bound XPO1 groove with ASB8 overlayed.

b, Comparison of XPO1 level when cells were treated with DMSO, Selinexor or KPT-396; XPO1 detected by WB and GAPDH used as loading control.

c-d, Same as in **a**, showing S109 and NCI-1.

e, A pull-down assay of XPO1 R197A by immobilized GST-ASB8•ELOB/C, in the absence/presence of KPT-185 or selinexor. Unbound proteins are shown in **Extended Data Figure 10c**.

f, A schematic depicting the allosteric degrader mechanism of selinexor. The left panel depicts high affinity, productive engagement of $CRL5^{ASB8}$ by selinexor-XPO1. The drug binds to half of the XPO1 groove, stabilizing the groove-open conformation and exposing the groove degron that makes many interactions with the substrate receptor ASB8, which also interacts with the adjacent h10-h11 degron. High affinity selinexor-XPO1-$CRL5^{ASB8}$ interactions lead to XPO1 ubiquitination and degradation by the proteasome. When the groove is closed or filled with NES or larger inhibitors, the groove degron is occluded. $CRL5^{ASB8}$ may interact only with the h10-h11 degron but the low affinity binding is unproductive for XPO1 degradation.

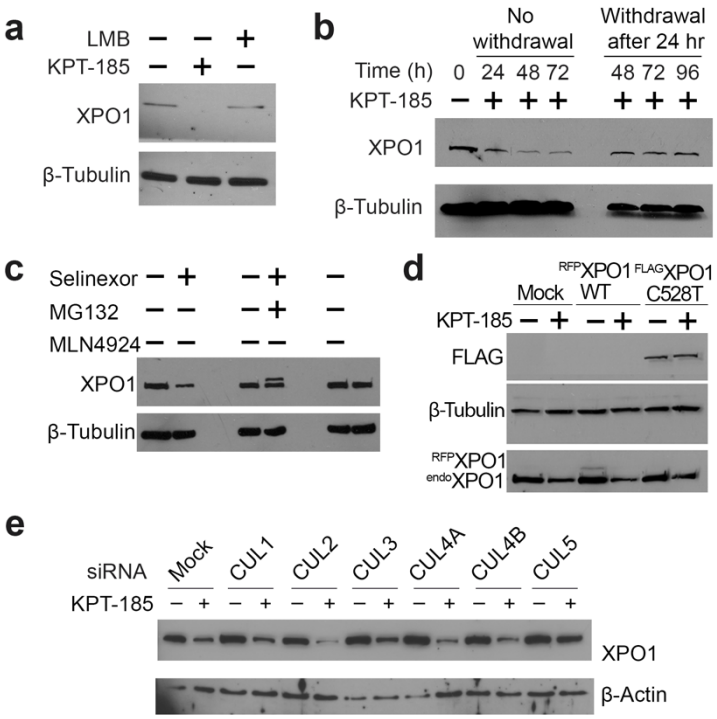

Extended Data Figure 1. KPT-185, but not LMB, causes CUL5-dependent degradation.

a, XPO1 levels in HT1080 cells treated with KPT-185, LMB or DMSO detected by Western blot.

b, HT1080 cells, treated with DMSO or KPT-185 for 24 h followed by fresh media with or without KPT-185, were collected at 24, 48 and 72 h for detection of XPO1 levels by Western blot (WB).

c, HT1080 cells treated with DMSO or selinexor for 2 h followed by MG132 or MLN4924 for the next 10 h and endogenous XPO1 detected by WB.

d, HT1080 cells transfected with $^{RFP}XPO1^{WT}$ or $^{FLAG}XPO1^{C528T}$ were treated with DMSO or KPT-185; XPO1 detected by WB. Loading control in **a-d** is β-tubulin.

e, HT1080 cells treated with siRNA for several cullins followed by treatment with DMSO or KPT-185. Loading control is β-actin.

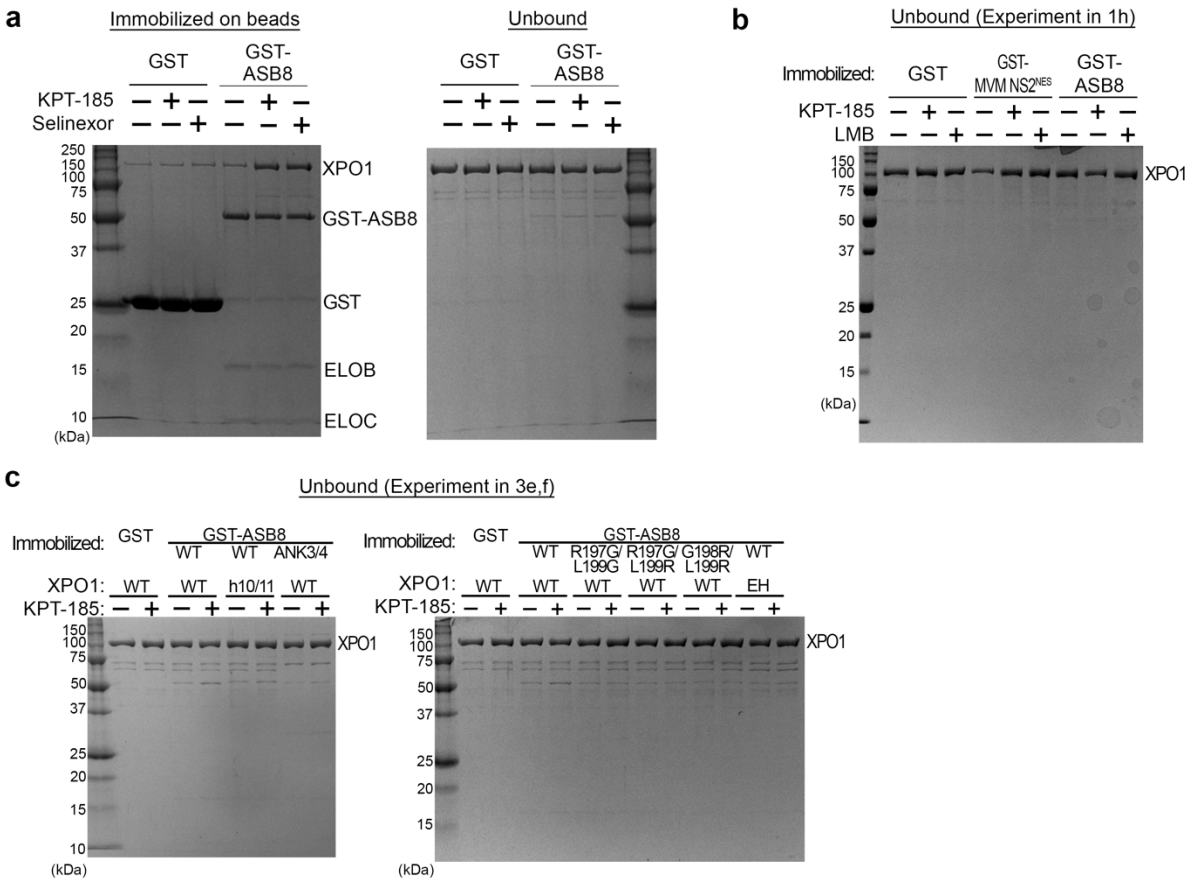

Extended Data Figure 2. Binding assays of GST-ASB8•ELOB/C with XPO1.

a, Pull-down assay of immobilized GST-ASB8•ELOB/C (negative control is GST) with XPO1 pre-treated with KPT-185 or selinexor. Bound and unbound proteins are visualized by Coomassie SDS-PAGE.

b, Unbound proteins from pull-down assay shown in **Figure 1h** of XPO1 treated with DMSO, KPT-185, LMB binding to immobilized GST-ASB8-ELOB/C (GST is negative control, and GST-MVM NS2^{NES} is positive control).

c, Unbound proteins from pull-down assay shown in **Figure 3e,f** of XPO1 (WT and mutants) in the presence/absence of KPT-185 binding to immobilized GST-ASB8-ELOB/C mutants. Gels were visualized by Coomassie staining.

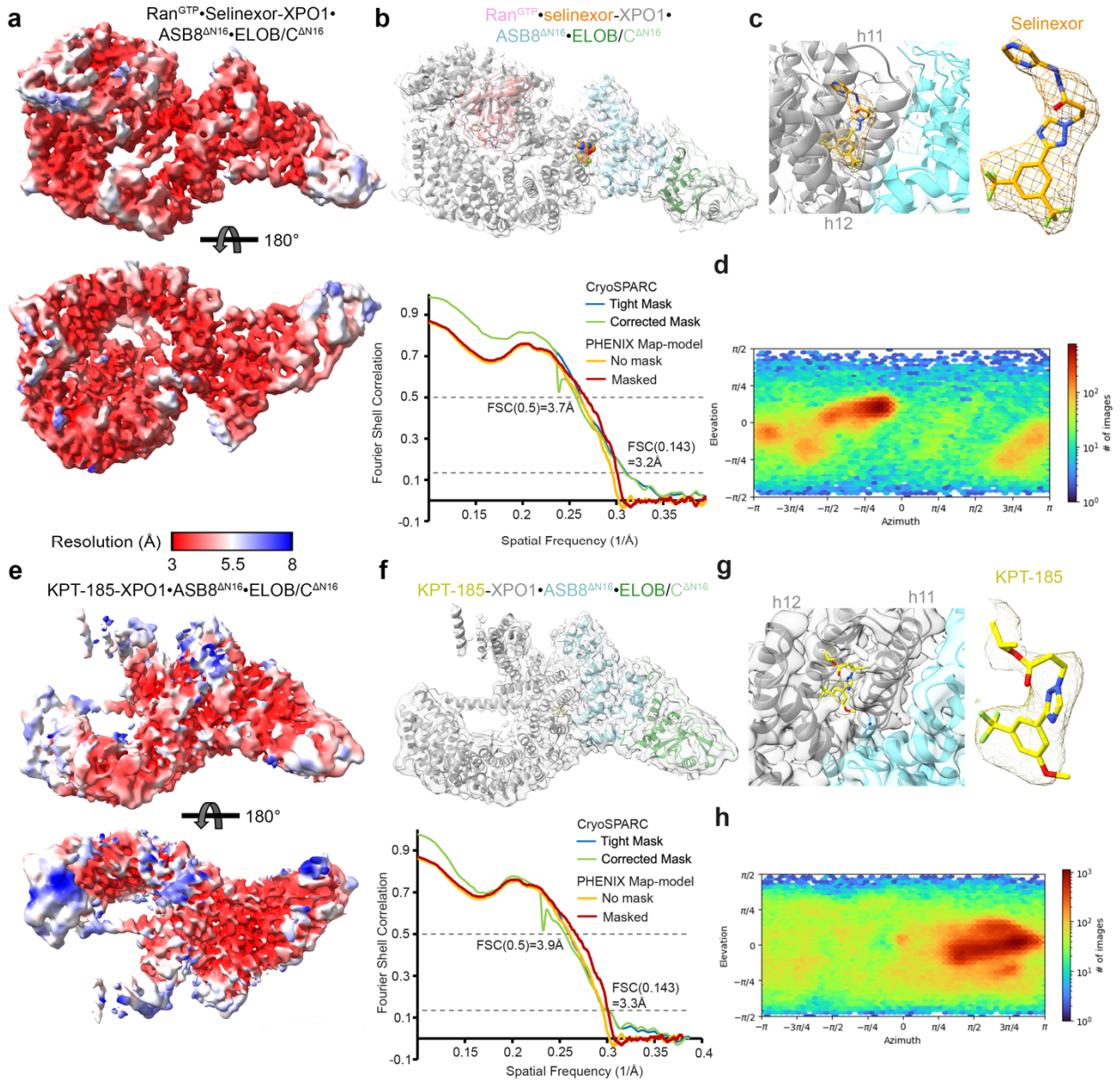

Extended Data Figure 3. CryoEM map and statistics for Ran^{GTP}•selinexor-XPO1•ASB8$^{\Delta N16}$•ELOB/C and KPT-185-XPO1•ASB8^{DN16}•ELOB/C.

a, The final map of Ran^{GTP}•selinexor-XPO1•ASB8$^{\Delta N16}$•ELOB/C colored by local resolution.

b, The refined Ran^{GTP}•selinexor-XPO1•ASB8$^{\Delta N16}$•ELOB/C structure overlayed with map in (**a**), accompanied by cryoSPARC and PHENIX map-model FSCs on the bottom.

c, A view of the selinexor(orange stick and mesh)-binding groove of XPO1 (gray surface and cartoon). ASB8 cartoon and map in cyan.

d, Viewing direction distribution plot for the particles used in reconstruction for map in (**a**).

e, The final map of KPT-185-XPO1•ASB8$^{\Delta N16}$-ELOB/C colored by local resolution as in (**a**).

f, Map and model statistics for KPT-185-XPO1•ASB8$^{\Delta N16}$-ELOB/C as in (**b**).

g, A view of the KPT-185 (yellow)-binding groove of XPO1 and ASB8 as in (**c**).

h, Distribution plot for the KPT-185-XPO1•ASB8$^{\Delta N16}$-ELOB/C particles as in (**d**).

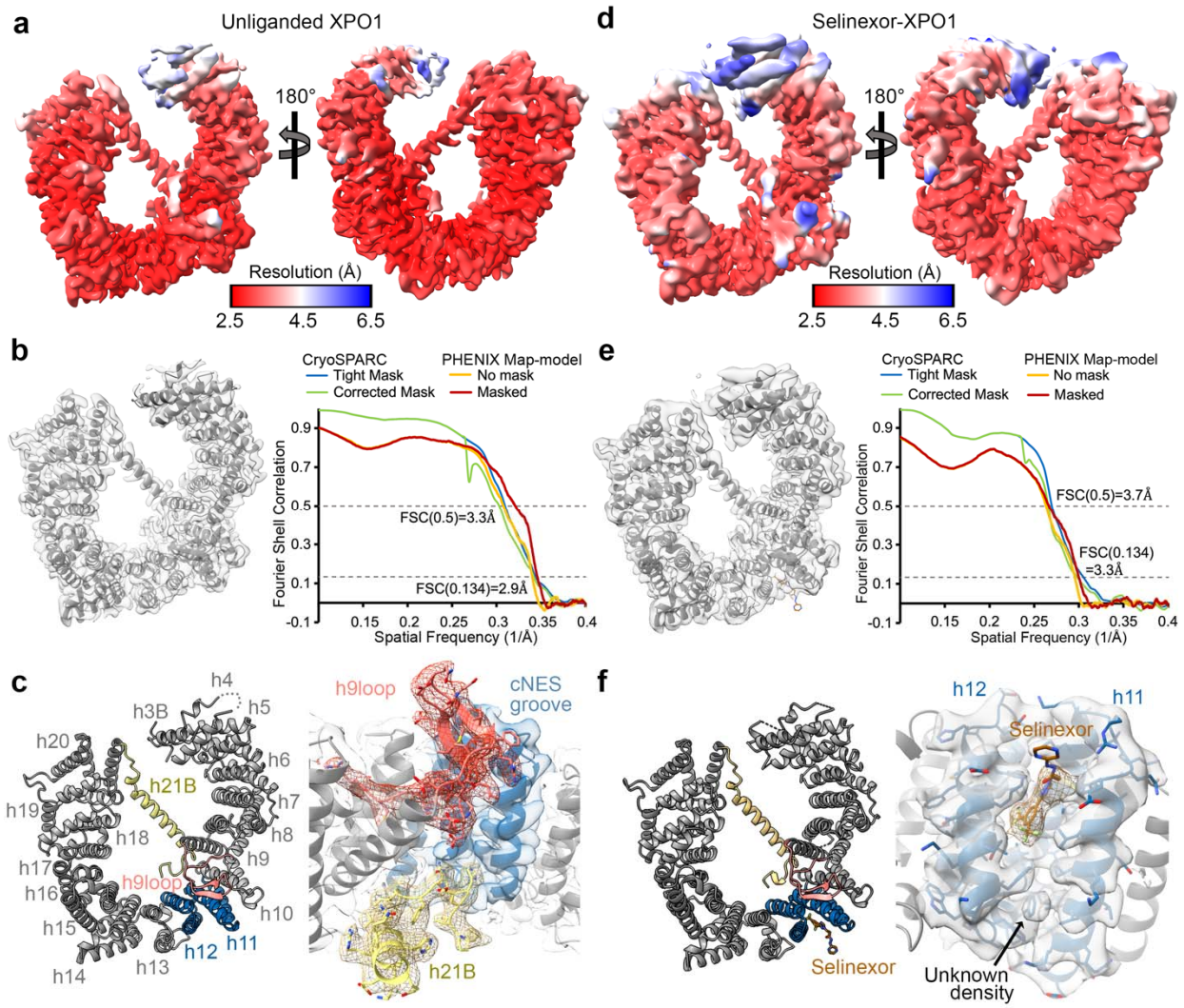

Extended Data Figure 4. CryoEM maps and statistics for unliganded XPO1 and selinexor-XPO1.

a, The final map of unliganded XPO1 colored by local resolution as indicated by the scale.

b, The refined structure of unliganded XPO1 in the final map, with the cryoSPARC and PHENIX generated map-model FSC curves.

c, Structure of unliganded XPO1. Left panel, the structure shown as cartoon, with the 21 HEAT repeats labeled. The panel on the right shows the density (mesh) of the h21B helix and C-terminal tail (yellow) and of the h9loop (red). The h21B-C-terminal tail stretch and the h9loop interact with the back (or concave side) of the cNES binding groove, which is shown in blue.

d, The final map of selinexor-XPO1 colored by local resolution.

e, The refined structure of selinexor-XPO1 in the final map, with the cryoSPARC and PHENIX generated map-model FSC curves.

f, The selinexor-XPO1 structure. Left, cartoon of XPO1 and selinexor shown as brown sticks. Right, the cryo-EM map at the selinexor-bound groove. The density for the KPT-185 scaffold of selinexor is well-defined, but density for the pyrazinylpropenehydrazide extension is weak. Extra density in the groove for an unknown molecule (possibly a water molecule or an ion) is marked with a black arrow.

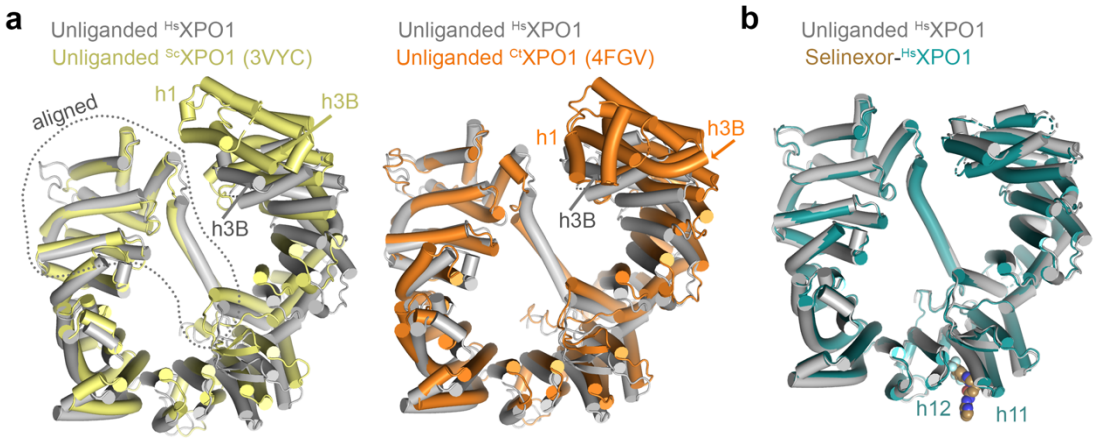

Extended Data Figure 5. Structural alignments at h18-h21 of several XPO1 structures.

a, Alignment of our unliganded XPO1 structure (grey) with: left, the crystal structure of unliganded *Sc* XPO1 (yellow, PDB ID: 3VYC) and right, the crystal structure of unliganded *Ct* XPO1 (orange, PDB ID: 4FGV). The width and pitch of the *Hs* and *Sc* XPO rings are similar, while the *Ct* XPO1 ring is larger and slightly more open.

b, Alignment of our unliganded XPO1 and selinexor-bound XPO1 cryo-EM structures. The two XPO1 solenoids are similar except for small differences at the N-terminal HEAT repeats and the cNES binding groove at h11 and h12 opens to accommodate selinexor (shown as spheres).

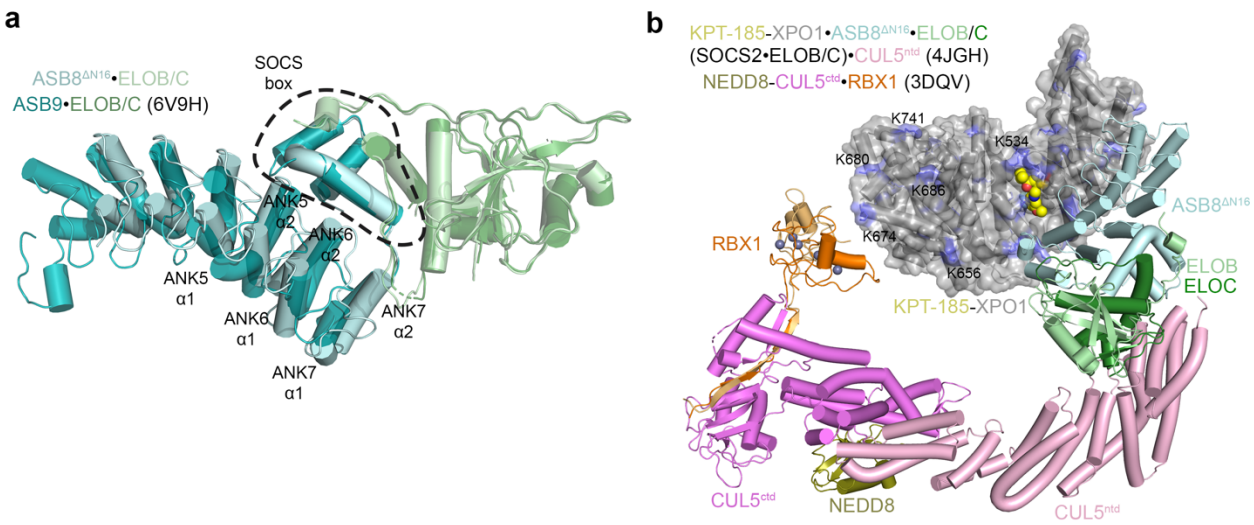

Extended Data Figure 6. KPT-185-XPO1•ASB8^{DN16}•ELOB/C: structural alignments.

a, Alignment of ASB8 and ASB9. ELOB/C (dark green) bound to ASB9 (dark teal) from 6V9H was aligned to ELOB/C (light green) bound to the ASB8 (pale cyan) in our KPT-185-XPO1•ASB8^{DN16}•ELOB/C cryo-EM structure (0.809 Å r.m.s.d.). The α1 and α2 helices of ANK5-7 are labeled, and the SOCS boxes are marked with a dashed line.

b, A model of KPT-185-XPO1•CRL5^{ASB8} generated by a series of alignments. The cryo-EM structure of KPT-185-XPO1•ASB8•ELOB/C was first aligned with ELOB/C-CUL5^{ntd} (4JGH) (r.m.s.d 1.151 Å). The overlayed ELOB/C-CUL5^{ntd} was then aligned to CUL5^{FL} (7ONI, r.m.s.d. 0.843 Å) to position the full length CUL5 into the model. Finally, the four-helix bundle and α/β subdomains (CUL5 residues 401-687) of the overlayed CUL5^{FL} (7ONI) and the NEDD8-CUL5^{ctd}•RBX1 (3DQV) were aligned (r.m.s.d. 1.143 Å) to model in the NEDDylated CUL5 and the released/mobile RBX1 (copies from both asymmetric units shown). The mobile RBX1/2 is expected to allow the associated E2 enzyme to reach exposed lysine residues of XPO1.

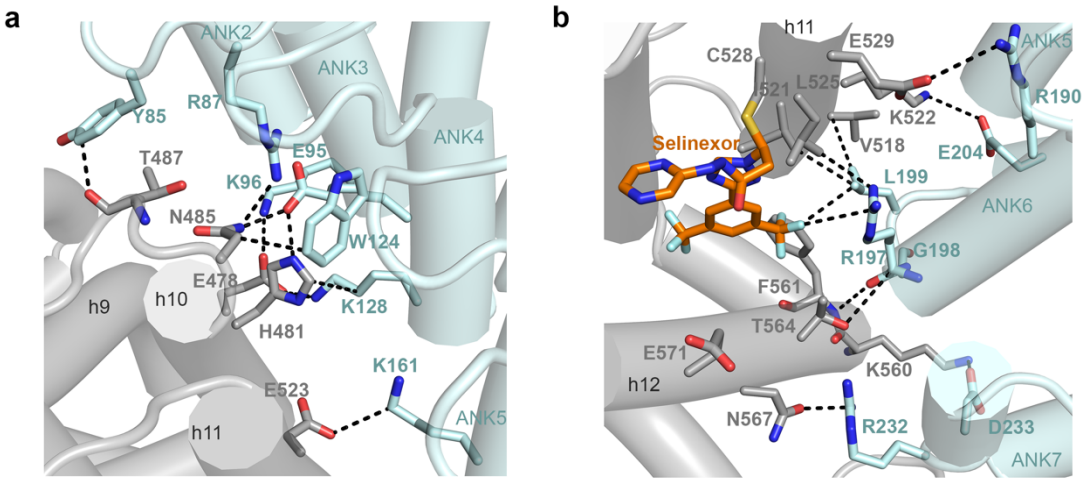

Extended Data Figure 7. The XPO1-ASB8 interaction interface in Ran^{GTP}•selinexor-XPO1•ASB8$^{\Delta N16}$•ELOB/C.

a, The XPO1-ASB8 h10/11-ANK3/4 interface. Dashed lines show contacts <4Å.

b, The XPO1-ASB8 h11/12-ANK6/7 interface. Left, dashed lines show contacts <4Å.

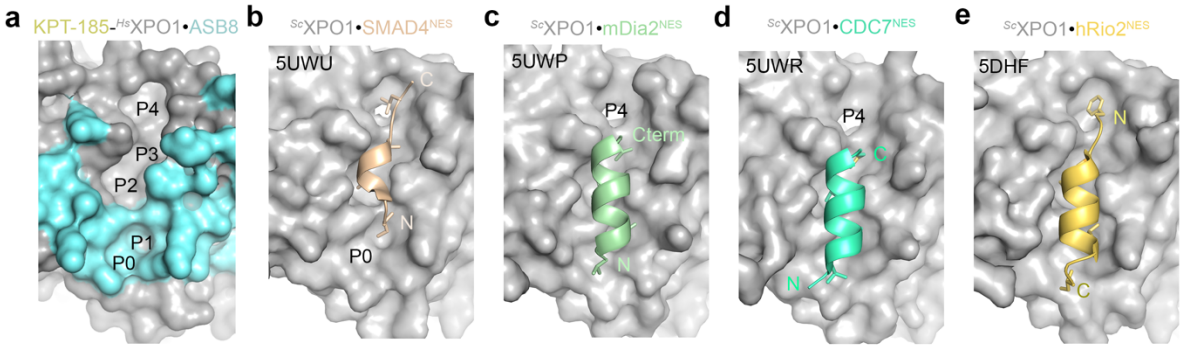

Extended Data Figure 8. The diverse structures of XPO1-bound NESs.

a, The NES/inhibitor binding groove of XPO1 from KPT-185-XPO1•ASB8•ELOB/C, with KPT-185 and ASB8 removed and to show the hydrophobic pockets P0-P4. The XPO1 surface is in gray and the interface with ASB8 interface colored cyan.

b-e, The XPO1 groove bound to different NES peptides, from four different crystal structures in the PDB: **b,** SMAD4^{NES} (light orange) binds P1-P4 leaving P0 exposed. **c,** mDia2^{NES} (light green) binds P0-P3 leaving P4 exposed, **d,** CDC7^{NES} (green-cyan) also leaves P4 exposed, and **e,** hRio2^{NES} (golden yellow) occupies the entire groove. All NESs studied thus far minimally bind P1-P3.

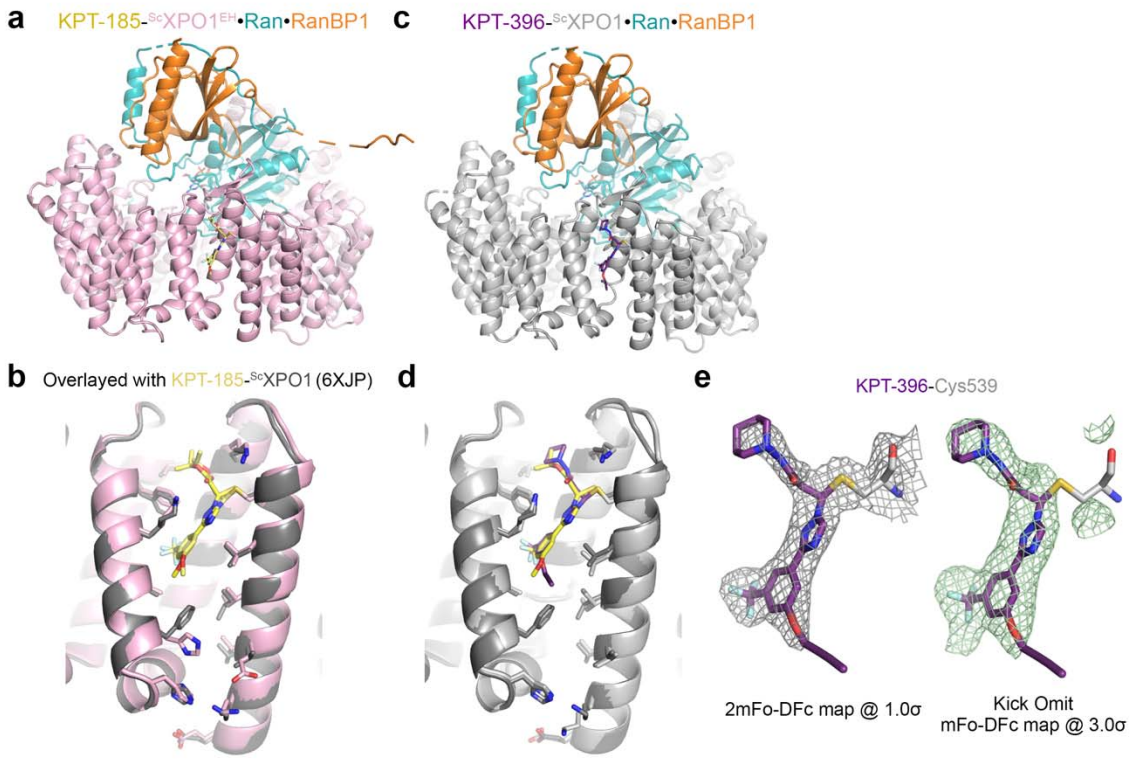

Extended Data Figure 9. X-ray crystallographic structures of inhibitor-bound ^{Sc}XPO1*•Ran^{GTP}•RanBP1.

a, The KPT-185-^{Sc}XPO1*^{EH}•Ran•RanBP1 structure where KPT-185 is shown as yellow sticks, and ^{Sc}XPO1*^{EH} (^{Sc}XPO1* is ^{Sc}XPO1 with humanized groove[23-26]), Ran^{GTP} and RanBP1 are shown as pink, teal and orange cartoon, respectively.

b, Zoom-in view of the KPT-185 bound groove in **a**, overlayed with the dark gray WT groove of the KPT-185-^{Sc}XPO1•Ran^{GTP}•RanBP1 crystal structure (PDB ID: 6XJP). The grooves of the mutant and WT XPO1 are highly similar except at the sites of the EH mutation.

c, The KPT-396-^{Sc}XPO1*•Ran^{GTP}•RanBP1 crystal structure where KPT-396 is shown as purple sticks, and ^{Sc}XPO1*, Ran^{GTP} and RanBP1 are shown as light gray, teal and orange cartoon, respectively.

d, Zoom-in view of the KPT-396 bound groove in **c**, overlayed with the KPT-185 bound groove (6XJP)**.**

e, Density for KPT-396 in the KPT-396-^{Sc}XPO1*•Ran^{GTP}•RanBP1 structure. KPT-396 and the conjugated Cys539 of ^{Sc}XPO1 (homologous to Cys528 of ^{Hs}XPO1) are shown with the 2mFo-Fc (gray mesh) or the kick omit map (green mesh). Density for the core scaffold of KPT-396 is strong but the density for the propynyl extension is poor. However, the propynyl extension is likely to point out of the groove towards solvent because of the alkyne bond.

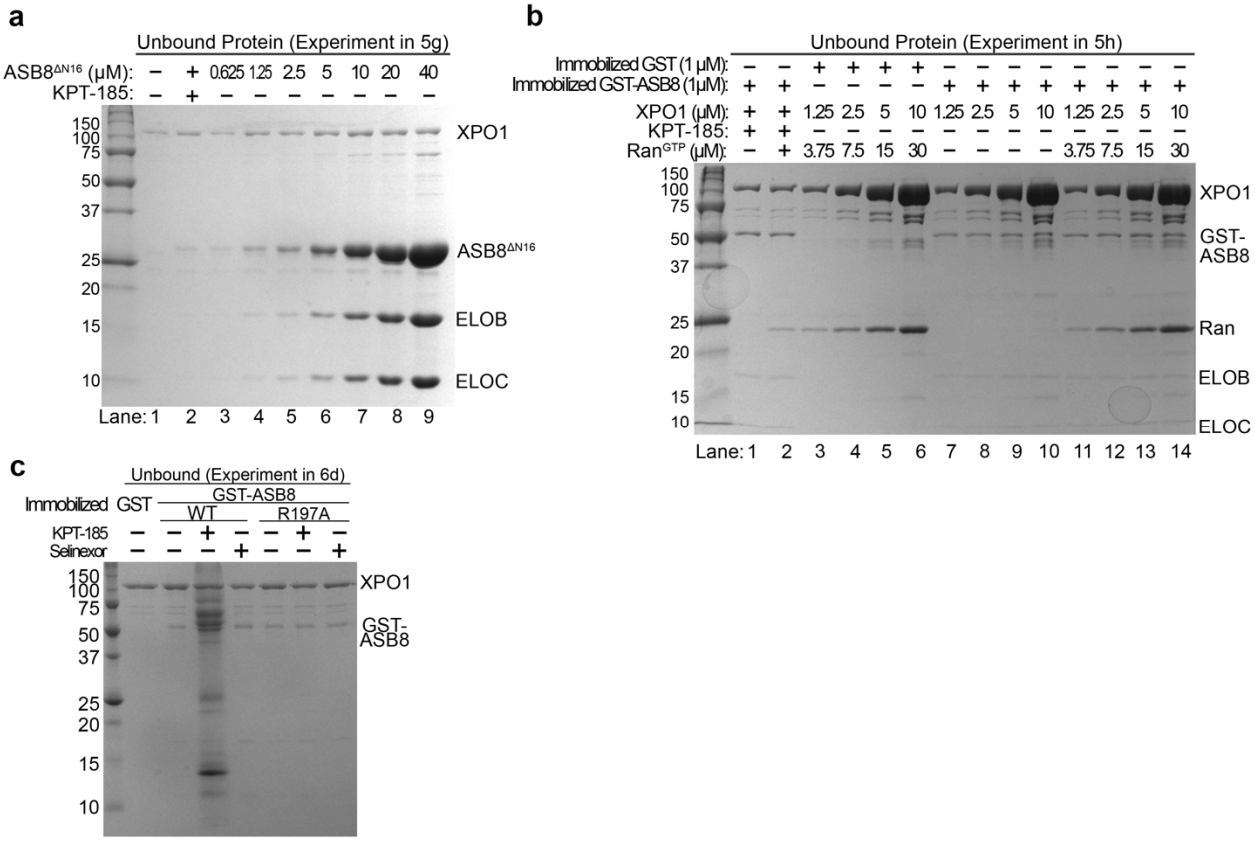

Extended Data Figure 10. Controls for binding assays of GST-ASB8•ELOB/C with XPO1 in absence of KPT-185.

a, Unbound proteins from the competition pull-down assay shown in **Figure 5g** of XPO1 binding to immobilized GST-NES (in the presence of Ran^{GTP}), in the absence/presence of $ASB8^{\Delta N16}$•ELOB/C and KPT-185.

b, Unbound proteins from the direct pull-down assay shown in **Figure 5h** of XPO1 binding to immobilized GST-ASB8•ELOB/C, in the absence/presence of KPT-185 and Ran^{GTP}.

c, Unbound proteins from pull-down assay shown in **Figure 6d** of XPO1 binding to immobilized GST-ASB8•ELOB/C, in the absence/presence of KPT-185 or selinexor.

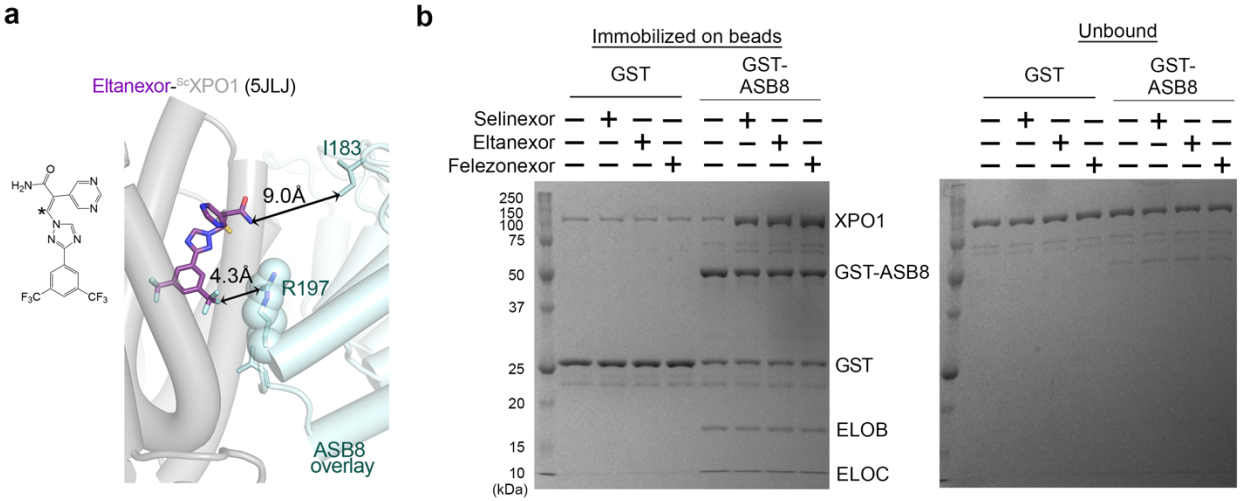

Extended Data Figure 11. Binding assay with other inhibitors

a, The chemical structure of eltanexor, and the eltanexor-bound XPO1 groove with ASB8 overlayed.

b, Pull-down assay of immobilized GST-ASB8•ELOB/C (negative control is GST) with XPO1 pre-treated with selinexor, eltanexor or felezonexor. Bound and unbound proteins are visualized by Coomassie SDS-PAGE.

Extended Data Table 1. Cryo-EM data collection and structure refinement

	Ran^{GTP}•selinexor-XPO1•$ASB8^{\Delta N16}$•ELOB/C	KPT-185•XPO1•$ASB8^{\Delta N16}$•ELOB/C	Selinexor•XPO1	Unliganded XPO1
Data collection and processing				
Microscope and detector	Titan Krios/ Gatan K3	Titan Krios/ Gatan K3	Titan Krios/ Gatan K3	Titan Krios/ Falcon 4
Magnification	105,000	105,000	105,000	165,000
Voltage (kV)	300	300	300	300
# of movies	4982	4746	5852	8568
Electron exposure ($e^-/Å^2$)	60	50	60	60
Defocus range (μm)	-0.9 to -2.4	-1.1 to -2.4	-0.9 to -2.2	-0.9 to -2.2
Pixel size (Å)	0.417	0.42	0.415	0.738
Symmetry imposed	C1	C1	C1	C1
# of particle extracted by Topaz	1,821,140	1,066,266	1,197,263	1,245,354
# of final particles	78,241	205,462	431,664	365,756
Map resolution (Å)	3.25	3.37	3.37	2.93
FSC threshold	0.143	0.143	0.143	0.143
CC_{mask}/CC_{volume}	0.79/0.79	0.78/0.78	0.80/0.80	0.85/0.85
Refinement and validation				
Initial model used	XPO1 (6TVO), Ran^{GTP} (3M1I), $ASB8^{\Delta N16}$•ELOB/C	Selinexor•XPO1, ASB8 (AF-Q9H765-F1 ELOB/C (6V9H)	Unliganded XPO1	XPO1 (3GB8)
Model resolution (Å)	3.1/3.2/3.8	3.3/3.4/3.8	3.2/3.3/3.7	2.8/2.9/3.1
FSC threshold	0/0.143/0.5	0/0.143/0.5	0/0.143/0.5	0/0.143/0.5
Model composition				
Nonhydrogen atoms	26296	9758	7421	7321
Protein residues	1629	1218	912	902
Ligand	3 (V6A, GTP, Mg)	1 (K85)	1 (V6A)	0
R.m.s. deviations				
Bond lengths (Å)	0.005	0.002	0.003	0.002
Bond angles (°)	0.836	0.491	0.559	0.426
Mean B-factors [ligand]	173.58 [92.5]	185.83 [142.95]	145.79 [20.0]	120.91
MolProbity score	1.82	1.33	1.36	1.18
Clashscore	9.21	5.98	6.54	3.88
Poor rotamers (%)	1.04	0	0	0
Ramachandran plot				
Favored (%)	95.42	98.50	98.23	98.65
Allowed (%)	4.15	1.50	1.66	1.35
Outliers (%)	0.43	0	0.11	0

Extended Data Table 2. X-ray crystallography data collection and refinement statistics.

Data collection		
	KPT-185-^{Sc}XPO1*^{EH}•Ran•RanBP1	**KPT-396-^{Sc}XPO1*•Ran•RanBP1**
Space group	$P4_32_12$	
Cell dimensions a=b, c (Å)	106.08, 303.93	105.58,304.56
Resolution range (Å)	50.00 – 2.37 (2.41 – 2.37)	50.00 – 2.41 (2.45 – 2.41)
Unique reflections	71232(3485)	66485 (3182)
Multiplicity	8.7(8.1)	8.3 (7.9)
Data completeness (%)	99.8 (99.3)	99.1 (95.9)
R_{merge}[a] /R_{pim}[b] (%)	8.9 (>100) / 3.4 (46.8)	9.8 (>100) / 3.4 (34.0)
I/σ(I)	19.4 (1.3)	19.2 (1.6)
$CC_{1/2}$ (last resolution shell)	0.509	0.772
Refinement statistics		
Resolution range (Å)	47.0 – 2.37 (2.43 – 2.37)	49.9 – 2.41 (2.47 – 2.41)
No. of reflections R_{work}/R_{free}	66477/2000 (2819/87)	60841/2000 (2296/78)
Data completeness (%)	93.2 (58.0)	90.5 (86.0)
Atoms (non-H protein/ligand & ions/H_2O)	10791/65/420	10869/84/403
R_{work}/R_{free} (%)	19.2/23.7 (28.3/29.9)	18.6/22.4 (27.8/24.0)
R.m.s.d. Bond length (Å)/angle (°)	0.003/0.483	0.002/0.462
Mean B-value (Å^2) Protein/ligands & ions/H_2O	47.4/38.4/37.1	46.2/44.4/36.7
Ramachandran plot (%)[b] (favored /disallowed)	97.5/0.08	97.4/0.15
ML coordinate error	0.31	0.28
Missing residues	A: 1-7, 188-193; B: 62, 69-77, 201; C: 970-985, 1054-1058	A: 1-7, 187-194; B: 62-78, 201; C: 686-689, 1054-1058
PDB code		

Data for the outermost shell are given in parentheses.

[a] $R_{merge} = 100\ \Sigma_h\Sigma_i|I_{h,i} - \langle I_h\rangle|/\Sigma_h\Sigma_i\langle I_{h,i}\rangle$, where the outer sum (h) is over the unique reflections and the inner sum (i) is over the set of independent observations of each unique reflection.

[a] $R_{pim} = 100\ \Sigma_h\Sigma_i\,[1/(n_h - 1)]^{1/2}|I_{h,i} - \langle I_h\rangle|/\Sigma_h\Sigma_i\langle I_{h,i}\rangle$, where n_h is the number of observations of reflections **h**.

[b] As defined by the validation suite MolProbity in PHENIX (Chen, V.B., Arendall, W.B.A., Headd, J.J., Keedy, D.A., Immormino, R.M., Kapral, G.J., Murray, L.W., Richardson, J.S., Richardson, D.C. (2010) *MolProbity*: all-atom structure validation for macromolecular crystallography. *Acta Cryst*. **D66**, 12-21.).

Methods

Constructs and expression vectors

Full-length wild type XPO1 was PCR amplified and subcloned into either into pciNeo-3xFLAG (gift from Dr. Xiaodong Wang, National Institute of Biological Sciences, Beijing) or into pTagRFP-C (Evrogen) mammalian expression vector to express ^{FLAG}XPO1 or ^{RFP}XPO1 fusion protein, respectively. XPO1 point mutant C528T variant was constructed by site directed PCR mutagenesis using the pciNeo-^{FLAG}XPO1 construct. In addition, full-length attB-flanked ^{FLAG}XPO1 was generated by PCR amplified from pCI-neo-^{FLAG}XPO1 construct and was introduced into pDONR233(Thermo Fisher Scientific) to create an entry vector for LR Gateway Reaction (Thermo Fisher Scientific). Subsequently pDONR233- ^{FLAG}XPO1 and destination vector pcDNA5/FRT/TO vector (Thermo Fisher Scientific) were used in LR reaction (Thermo Fisher Scientific) as manufacturer's instructions to generate pcDNA5/FRT- ^{FLAG}XPO1 FRT integration vector. Ubiquitin B (UBB) in pENTR221 vector was purchased as an Ultimate ORF clone (Thermo Fisher Scientific, clone ID IOH56688), PCR amplified and inserted into pcDNA3.1-HA (gift from Oskar Laur (Addgene plasmid # 128034; http://n2t.net/addgene:128034; RRID:Addgene_128034)) to express ^{HA}Ub fusion protein. All constructs were made using standard molecular procedures and validated by direct Sanger sequencing.

Cell culture and transfection

Human fibrosarcoma HT1080 were grown in complete Dulbecco's modified Eagle's medium (D-MEM, Thermo Fisher Scientific) supplemented with 10% heat inactivated fetal calf serum penicillin/streptomycin (100 U/ml) and 2 mM glutamine). Flp-

In T-REx-293 Cell Line (Thermo Fisher Scientific) was maintained in complete D-MEM supplemented with 15 µg/ml blasticidin and 100 µg/ml zeocin (InvivoGen). HEK 293 T-REx ^{FLAG}XPO1 stable cell line maintained in the complete D-MEM culturing medium supplemented with 10 µg/ml blasticidin and 50 µg/ml hygromycin (InvivoGen). All transfections were carried out using either Lipofectamine2000 (plasmid) or Lipofectamine RNAiMAX (siRNA) according to manufacturer's instructions.

Immunoblotting

Briefly, samples of proteins were prepared using either RIPA buffer (25 mM Tris-HCl, pH 7.5, 150 mM NaCl, 1% NP-40, 1% sodium deoxycholate and 0.1% SDS and 1x cOmplete protease inhibitors (Roche) or NET-150 (150 mM NaCl, 20 mM Tris at pH.8.0, 1 mM EDTA, 1x NaF/Na-orthovanadate (10 mM/ 1mM), 0.5 % NP-40, 1x cOmplete protease inhibitors). 10 µg portion of total lysates were resolved by SDS-PAGE and transferred to a PVDF membrane. The membrane was blocked for 1 h in 5% non-fat milk and incubated with primary antibody for another 1 h at room temperature. The membranes were then incubated with horseradish peroxidase-conjugated anti-mouse or anti-rabbit IgG (1:10,000; Thermo Fisher Scientific). Finally, the membranes were developed using a Kodak medical X-ray processor (Kodak, Rochester, NY, USA) or Gel Doc XR+ Gel Documentation System (Promega).

Generation of the HEK 293 T-REx ^{FLAG}XPO1 stable cell line

Flp-In T-REx-293 cells (Thermo Fisher Scientific) were co-transfected with Flp recombinase expression vector pOG44 (Thermo Fisher Scientific) and pcDNA5/FRT-^{FLAG}XPO1 or pcDNA5/FRT construct. To select stable HEK 293 T-Rex ^{FLAG}XPO1 cell lines derived from the host cell line by FLP mediated integration into the FRT docking

site, zeocin was substituted with 50 µg/ml hygromycin B. ^{FLAG}XPO1 expression was induced by supplementing growth media with 0.5µg/ml doxycycline (Sigma Aldrich).

Pulse-chase labeling of endogenous XPO1 protein in HT1080 cells

HT1080 cells were grown 50% confluency and incubated with high glucose, no glutamine, no methionine, no cystine DMEM (Gibco, #21013024) supplemented with 1x L-glutamine (Gibco, #35050061) for 2 h. The cells were then pulsed for 1 h with 200 µCi/ml of [35S]-Met(methionine)/[35S]-Cys(Cysteine) (Perkin Elmer, NEG072002MC) and chased for 0, 12 , 24, 27, 30, 33, 36 and 48 h. After each chase period the cells were lysed in RIPA buffer and XPO1 protein was recovered from whole lysates by immunoprecipitation using mouse monoclonal XPO1 antibody (Santa Cruz Biotech, sc-5595) and subjected to SDS-polyacrylamide gel electrophoresis. Gel was dried for 2 h and exposed to 35S intensifying screen and X-OMAT film in 70 °C for 24 h. The band corresponding to XPO1 was identified by autoradiography, and band intensities were calculated using ImageJ[65].

In vivo XPO1 degradation by SINE compound treatment

Human fibrosarcoma HT1080 cells and tetracycline-inducible HEK 293 T-REx ^{FLAG}XPO1 cells were cultured in complete D-MEM and grown to 80% confluence. Where indicated, HT1080 cells were transiently transfected with the indicated RFP or FLAG-^{Hs}XPO1 constructs and recovered in fresh media for 12 h before KPT-185 treatment. Unless otherwise indicated, cells were treated with 500 nM KPT-185, 1 µM selinexor or 10 nM LMB, and cells were grown for another 18-72 h. When needed MG132 or MLN4924 was added to growth media to 200 µM or at 100 µM final concentration. Cells were collected by centrifugation and lysed on ice for 30 min in RIPA buffer.

Immunoblotting was used to detect XPO1 (CRM1 rabbit polyclonal H-300; sc-5595, Santa Cruz or CRM1 mouse monoclonal (C-1): sc-74454, Santa Cruz) and β-actin or β-tubulin (Loading Control Antibody Sampler Kit #5142, Cell Signaling Technology) to confirm equal protein loading.

Detection of ^{HA}Ub-XPO1 conjugation

HEK 293 T-REx ^{FLAG}XPO1 cells were reverse transfected with pcDNA3.1-^{HA}Ub or pcDNA3.1-HA and grown in complete D-MEM in the presence of doxycycline. Cells were then treated with DMSO, 0.5 µM KPT-185 and 200 µM MG132, or 200 µM MG132 alone for additional 18 h before lysis. Cells were collected by centrifugation and lysed on ice for 30 min in RIPA buffer. ^{HA}Ub-^{FLAG}XPO1 conjugation and total ^{FLAG}XPO1 proteins were immunodetected by using primary antibodies for HA tag (Thermo Fisher Scientific, #26183) or FLAG M2 tag (Sigma Aldrich, F3165), respectively.

In vitro deubiquitination assay

HEK 293 T-REx ^{FLAG}XPO1 cells were grown in complete D-MEM in the presence of doxycycline to 80% confluence. Cells were then treated with 1 µM KPT-330 and 0.2 µM MG132 for additional 18 h before lysis. Cells were collected by centrifugation and lysed on ice for 30 min in NET-150 buffer. ^{FLAG}XPO1 protein was recovered from whole lysates by immunoprecipitation using anti-FLAG M2 magnetic beads (Sigma Aldrich) and eluted by competition using the 3X FLAG peptide (APExBio) in TE buffer pH 8.0 (10 mM Tris, 1 mM EDTA). Subsequently, half of the elute was incubated with vOTU in DUB buffer (50 mM NaCl, 50 mM Tris, pH 7.5 and 50 mM DTT) for 30 min at RT. Immunoblotting with FLAG M2 antibody (Sigma Aldrich, F3165) was used to detect ^{FLAG}XPO1 levels.

siRNA knockdowns

ON-TARGETplus siRNA targeting the mRNAs for NAE1 (MU-006401-02) and CUL5 (MU-019553-01) was purchased from Dharmacon, Horizon Discovery, and MISSION esiRNA targeting the mRNAs for ELOB (EHU150621), ELOC (EHU903091), RBX1 (EHU055711) and RBX2 (EHU094071) were purchased from Sigma Aldrich. The negative control scrambled siRNA was Dharmacon, Horizon Discovery (D-001210-01). siRNAs were transfected into cells with Lipofectamine RNAiMAX (Thermo Fisher Scientific), according to the manufacturer's instructions at 30 nM final concentration. The most efficient knockdown at protein levels was seen 48 h without compromising cell's integrity. XPO1 degradation by KPT-185 treatment were performed at day 3 after knockdown. 18 h post-KPT-185 treatment, cells were lysed in RIPA buffer and immunoblotting was performed using primary antibodies: XPO1 (CRM1 rabbit polyclonal H-300; sc-5595, Santa Cruz or CRM1 mouse monoclonal (C-1): sc-74454), NAE1 (Cell Signaling Technology, #14321), ELOB (Proteintech, 12450-1-AP), ELOC (Bethyl Laboratories, A304-008A), CUL5 (Bethyl Laboratories, A302-173A), RBX1 (Cell Signaling Technology, #11922), RBX2 (Sigma Aldrich, HPA036995) and GAPDH (Loading Control Antibody Sampler Kit #5142, Cell Signaling Technology).

Patient Sample Processing, Cell Lines, and Cell Culture

Blood was obtained from healthy volunteers or patients with CLL following written informed consent under a protocol approved by the Institutional Review Board of The Ohio State University (OSU; Columbus, OH) in accordance with the Declaration of Helsinki. All patients examined had CLL as defined by the 2008 International Workshop on Chronic Lymphocytic Leukemia criteria, and cells were isolated and cultured as

previously described[23]. HG-3 (DSMZ, Germany), cells were cultured in RPMI 1640 (Gibco) supplemented with 10% fetal bovine serum (FBS, VWR) and 1% penicillin/streptomycin/L-glutamine (P/S/G; Gibco) at 37 °C and 5% CO_2. Cell lines were validated via short tandem repeat analysis by The Ohio State University Genomic Services Core. For experiments cells were resuscitated, cultured in RPMI (Invitrogen) supplemented with 10% fetal bovine serum (FBS), and used within 3 to 4 weeks from thawing. All cell lines were confirmed to be *Mycoplasma* negative using the MycoAlert Mycoplasma Detection Kit from Lonza according to the manufacturer's instructions and used within 3 to 4 weeks from thawing. Cells were lysed in RIPA buffer. Proteins were separated by SDS-PAGE and blots probed with commercially available antibodies and detected by addition of Enhanced chemiluminescence (ECL) substrate (Pierce) followed by quantification by Chemi-Doc system with Quantity One software (Bio-Rad Laboratories). XPO1 used SC-74454, 1:1000 dilution, full ECL. ASB8 used Invitrogen MA5-26984, 1:500 dilution, 50% ECL; GAPDH using SC-47724 ab, 1:1000 dilution, 50% ECL.

Protein expression and purification

Full-length XPO1 was purified according to established protocol[66]. Human ASB8 cDNA in pENTR221 vector was purchased as an Ultimate ORF clone (Thermo Fisher Scientific, clone ID IOH3117), PCR amplified and inserted into pGEX-4T3 (Amp^R) vector with a TEV protease site. Human ELOB (full-length) and ELOC (residues 17-112) were obtained in pACYC (Cam^R) (gift from Dr. Elizabeth Komives). ASB8 plasmids were co-transformed into BL21-gold(DE3) *E. coli* competent cells containing pACYC-ELOB/C for co-expression of GST-ASB8•ELOB/C. Cultures were grown in LB media at 37 °C to an

OD_{600} ~0.7 and induced with 0.4 μM IPTG at 18 °C for 18 hours. Cells were pelleted by centrifugation at 4,500 x g for 30 minutes at 4 °C, resuspended in buffer (50 mM HEPES pH 7, 150 mM NaCl, 10% glycerol, 2 mM DTT, 5 mM EDTA, 5 mM EGTA) supplemented with 200 μg/mL Pefabloc, 10 μg/mL leupeptin, and 1 mM benzamidine protease inhibitors, and then lysed with the EmulsiFlex-C5 cell homogenizer (Avestin). GST-ASB8•ELOB/C was purified over Glutathione Sepharose 4B (GSH; GE Healthcare) resin followed by size exclusion chromatography (SEC) over a Superdex200 10/300 Increase column (Cytiva) pre-equilibrated in TB buffer (20 mM HEPES pH 7.4, 110 mM KOAc, 2 mM $Mg(OAc)_2$, 10% glycerol, 2 mM DTT). $ASB8^{\Delta N16}$ and all ASB8 mutants were expressed and purified using the same protocol. GST-$ASB8^{\Delta N16}$•ELOB/C was cleaved from GSH-Sepharose resin by TEV protease for 1 hr at room temperature prior to SEC. Ran^{GTP} was purified according to previous published method protocol[66], his tag was not cleaved.

In vitro binding assays

In vitro pull-down binding assays were performed by incubating 0.5 μM GST, GST-$NES^{MVM\ NS2}$, or GST-ASB8 (WT or mutants) ± 1 μM XPO1 (WT or mutants) ± DMSO, 2 μM inhibitor (KPT-185, selinexor, eltanexor, felezonexor or LMB) with 20 μL GSH-Sepharose beads (bead bed volume) (Cytiva) in a 200 μL reaction in TB Buffer for 30 min at 4°C. For competition binding assays, 0.5 μM XPO1 ± 1.5 μM Ran^{GTP} ± 1 μM KPT-185 was added to 20 μL GSH-Sepharose beads with GST-$SNUPN^{NES}$ from bacterial lysates, and $ASB8^{\Delta N16}$•ELOB/C was titrated from 0.625 – 40 μM. For direct binding assays, 1 μM GST or GST-ASB8•ELOB/C ± 2.5 μM KPT-185 + XPO1 titrated from 1.25 – 10 μM ± Ran^{GTP} titrated from 3.75 – 30 μM was used. All samples were

washed three times with 500 µL TB buffer, and bound proteins were separated and visualized by SDS-PAGE gel stained with Coomassie stain. All binding assays were repeated in triplicates.

Cryo-EM sample preparation and data collection

For KPT-185-XPO1•ASB8$^{\Delta N16}$•ELOB/C, 2mg of XPO1 was mixed with GST-ASB8$^{\Delta N16}$-ELOB/C and KPT-185 (1:2:2 molar ratio) and 1 mg of TEV protease in TB buffer (20 mM HEPES pH 7.4, 110 mM KOAc, 2 mM $Mg(OAC)_2$, 2 mM DTT, 10% glycerol) for 1 hour at room temperature, then passed over GSH-Sepharose resin. Flowthrough was concentrated to 1 mL. For Ran^{GTP}•selinexor-XPO1•ASB8$^{\Delta N16}$•ELOB/C, 2mg of XPO1 was mixed with ASB8$^{\Delta N16}$-ELOB/C with no GST tag, Ran^{GTP} and KPT-185 (1:2:2:2 molar ratio). Both protein samples were purified over a Superdex200 10/300 Increase column (Cytiva) pre-equilibrated in cryo-EM buffer (20 mM HEPES pH 7.4, 150 mM NaCl, 2 mM $Mg(OAc)_2$, 2 mM TCEP). 4 µL of complex sample (0.4 mg/ml of KPT-185-XPO1•ASB8$^{\Delta N16}$•ELOB/C supplemented with 2-fold excess KPT-185, or 0.5 mg/ml of Ran^{GTP}•selinexor-XPO1•ASB8$^{\Delta N16}$•ELOB/C supplemented with 2-fold excess ASB8$^{\Delta N16}$-ELOB/C and selinexor) was applied to a 400-mesh copper grid (Quantifoil R1.2/1.3). For unliganded XPO1, XPO1 was buffer exchanged into cryo-EM buffer and diluted to 3.4 mg/mL and supplemented with 0.025% Tyloxapol (BioVision). For Selinexor-XPO1, XPO1 was diluted to 3 mg/mL with two times molar excess of Selinexor and supplemented with 0.025% Tween-20 (BioVision). 4 µL of each sample were applied on Quantifoil R1.2/1.3, 300 mesh copper grids. All grids were pre-glow-discharged using a PELCO easiGlow glow discharge apparatus (Ted Pella) at 30 mA for

80 s. Excess sample was blotted and plunge frozen in liquid ethane using the Vitrobot Mark IV System (Thermo Fisher) at 4 °C with 95% humidity.

One Ran^{GTP}•selinexor-XPO1•ASB8$^{\Delta N16}$•ELOB/C grid was used for 24 hr data collection at the UT Southwestern Cryo-Electron Microscopy Facility (CEMF) on a Titan Krios microscope (Thermo Fisher) at 300 kV with a Gatan K3 detector in non-correlated double sampling (CDS) super-resolution mode using SerialEM software[67].One KPT-185-XPO1•ASB8$^{\Delta N16}$•ELOB/C grid and one Selinexor-XPO1 grid were used for 18 and 24 hr data collection, respectively, at the CEMF with CDS-mode. One unliganded XPO1 grid was used for 24 hr data collection on a Titan Krios 300kV microscope equipped with Falcon 4 detector at the CEMF. More details are listed in **Extended Data Table 1**.

Cryo-EM data processing and structure determination

All data processing was performed using the software cryoSPARC v4.2 or 4.4[68]. Movies were imported, subjected to patch motion correction and patch CTF estimation. For Ran^{GTP}•selinexor-XPO1•ASB8$^{\Delta N16}$•ELOB/C, KPT-185-XPO1•ASB8$^{\Delta N16}$•ELOB/C and Selineor-XPO1 dataset, a ½ F-crop factor was applied during patch motion correction.

For KPT-185-XPO1•ASB8$^{\Delta N16}$•ELOB/C, initial blob picking was performed on 795 micrographs and followed by two rounds of 2D classification to obtain templates used for template picking on the full dataset, which resulted in 2,386,555 particles. After two rounds of 2D classification, 627,555 particles were split into three classes for ab-initio reconstruction and further classified using heterogeneous refinement. One class had a 4.96A map showing helical features resembling XPO1 and ASB8 (193,789 particles). To obtain more particles, these particles were used to train Topaz[69], which picked 1,066,266 particles. After rounds of 2D classification, the remaining 770,623 particles

were used for ab-initio reconstruction and heterogeneous refinement, seeking four classes. One class (205,462 particles) resembled the initial map used to train Topaz and was subsequently refined to 3.37 Å using Non-Uniform (NU) refinement with optimization of the per-exposure-group CTF parameters (defaults and spherical aberration).

For Ran^{GTP}•selinexor-XPO1•$ASB8^{\Delta N16}$•ELOB/C, template was generated using the initial model and used for template picking on full dataset, which resulted in 1,424,491 particles. After 1 round of 2D classification and 3 rounds of 3D heterogenous refinement, particle stack of 171,837 particles were used for Topaz training, which yielded 1,821,140 particles. After 1 round of 2D classification and 6 additional rounds of 3D heterogenous refinement (with 2 classes to clean up junk particles), 78,241 particles were used in NU after global CTF refinement with default parameters for 3 iterations, which yielded the best resolution map at 3.25 Å.

For unliganded XPO1 micrographs, blob picker was used to select 3,643,569 initial particles. After 4 rounds of 2D classification, 851,026 particles were used to obtain 3 *ab initio* models, which were subsequently submitted to heterogeneous refinement. ~36% of the particles partitioned into a map that looks like intact XPO1, which were used to train Topaz for picking 1,245,354 initial particles. After 1 round of 2D classification, particles were classified into the previous 3 classes by heterogeneous refinement. 375,108 particles (50% out of the final 753,568 particles) were intact and subjected to final NU refinement with optimizations of pre-particles defocus and per-group CTF parameters (Tilt, Trefoil, Spherical Aberration and Anisotropic Magnification) to yield final map of 2.93 Å resolution.

For Selinexor-XPO1 micrographs, templates were generated using unliganded XPO1 particles and template picker was used to select 4,541,251 initial particles. After 7 more rounds of 2D classification, 688,481 particles were used to obtain 4 *ab initio* models, which were submitted to heterogeneous refinement. ~42% of the particles partitioned into a map that looks like intact XPO1. The good particles were used to train Topaz for picking, which extracted 1,197,263 initial particles. After 3 rounds of 2D classification, particles were classified into the previous 4 classes by heterogeneous refinement. 431,664 particles (52% out of the final 829,704 particles) were subjected to local CTF refinement and then a final NU refinement with optimizations of the pre-particle defocus and per-group CTF parameters (Tilt and Trefoil only) to yield final map of 3.37 Å resolution.

Cryo-EM model building, refinement and analysis

All initial models (specified in **Extended Data Table 1**) were roughly docked into unsharpened maps using UCSF Chimera or ChimeraX[70,71] and then subjected to real-space refinement with global minimization and rigid body restraints in Phenix[72] and manual model building using ISOLDE[73] and Coot[74]. Model validation was performed in Phenix. For KPT-185-XPO1•ASB8$^{\Delta N16}$•ELOB/C, deepEMhancer[75] was used to generate maps to assist in modeling of N- and C-terminal HEAT repeats of XPO1. For Selinexor-XPO1, KPT-185-XPO1•ASB8$^{\Delta N16}$•ELOB/C and Ran^{GTP}•selinexor-XPO1•ASB8$^{\Delta N16}$•ELOB/C, the Cys528-selinexor/KPT-185 conjugation was restrained to be 1.8 Å long during real-space refinement in Phenix to aid placement of the inhibitor and the cysteine sidechain. The location of Selinexor was optimized by manual building in the final step as the density for the ligand does not cover the whole inhibitor.

Structures were analyzed using PyMOL 2.4 and 2.5[76], PDBe PISA for the binding interface[77]. and the APBS electrostatic plugin for 3D structure and electrostatic analysis[76,78]. All figures were generated using PyMOL or ChimeraX.

X-ray structure determination

Protein purification, complex formation, crystallization of KPT-185-^{Sc}XPO1^{EH}•Ran•RanBP1 and KPT-396-^{Sc}XPO1•Ran•RanBP1 were all performed according to published protocol[79]. KPT-185 was used in 2 times molar excess while KPT-396 was used at 5 times excess. Both complexes were concentrated to ~10 mg/mL. Crystals were formed overnight using hanging-drop method in crystallization condition of 17% PEG3350, 100 mM Bis-Tris (pH 6.6) and 200 mM ammonium nitrate and cryoprotected with 23% PEG3350 and 12% (v/v) glycerol for freezing. X-ray diffraction data was collected at Advanced Photon Source – Structural Biology Center 19ID beamline and processed using HKL3000[80]. Structure models were generated by refining 4GMX as starting model against the collected data using PHENIX[72,81,82]. X-ray/stereochemistry and X-ray/ADP weight were optimized by phenix.refine in later steps. Manual building was performed in Coot[83].

XPO1 degradation assay with Simple Western

HEK293T cells (ATCC) were transiently (co-)transfected with pDNA expressing XPO1 or ASB8 (wild type or mutant) using Turbofectin 8.0 (OriGene) according to the manufacturer's protocol. After 24 hrs, media were replaced with fresh media containing KPT-330 as indicated and 10 µM Q-VD-OPh. After another 24 hrs, cells were collected and lysed in RIPA buffer (Thermo Fisher Scientific) containing 1× HALT Protease Inhibitor Cocktail (Thermo Fisher Scientific). We used a Simple Western size assay

(JESS, ProteinSimple) for immunodetection of XPO1 (NB100-79802, Novus, 1:1000) and β-tubulin (NB600-936, Novus, 1:40). Data analysis was done with Compass for Simple Western software (ProteinSimple). For quantification, we first determined the ratio of XPO1/β-tubulin peak area and then normalized to the 0 nM KPT-330 lane within each transfection condition.

Cell viability assay

HAP1 cells (Horizon Discovery) were transduced at low multiplicity of infection (MOI<0.1) with a lentiviral vector for stable overexpression of either wild type or mutant ASB8. Cells were treated with a serial dilution of KPT-330 for a period of three days. Next, 20 µL MTS reagent (CellTiter 96 Aqueous Non-Radioactive Cell Proliferation Assay from Promega) was added and cells were incubated for an additional 2 hrs after which absorbance was measured at 490 nm with a Safire 2 microplate reader (Tecan). For each drug concentration, the absorbance values of three replicate wells were averaged, blank corrected and normalized to those of untreated cells. Dose-response curves were obtained by fitting a non-linear, four-parameter regression model to relative cell viability values using GraphPad Prism 10.

Data availability statement

Coordinates and density maps or structure factors will be deposited in the Protein Data Bank and Electron Microscopy Data Bank prior to publication. All data are available upon request.

References

1 Wing, C. E., Fung, H. Y. J. & Chook, Y. M. Karyopherin-mediated nucleocytoplasmic transport. *Nat Rev Mol Cell Biol* **23**, 307-328 (2022). https://doi.org/10.1038/s41580-021-00446-7

2 Azmi, A. S., Uddin, M. H. & Mohammad, R. M. The nuclear export protein XPO1 - from biology to targeted therapy. *Nat Rev Clin Oncol* **18**, 152-169 (2021). https://doi.org/10.1038/s41571-020-00442-4

3 De Cesare, M. *et al.* Anti-tumor activity of selective inhibitors of XPO1/CRM1-mediated nuclear export in diffuse malignant peritoneal mesothelioma: the role of survivin. *Oncotarget* **6**, 13119-13132 (2015). https://doi.org/10.18632/oncotarget.3761

4 Tai, Y. T. *et al.* CRM1 inhibition induces tumor cell cytotoxicity and impairs osteoclastogenesis in multiple myeloma: molecular mechanisms and therapeutic implications. *Leukemia* **28**, 155-165 (2014). https://doi.org/10.1038/leu.2013.115

5 Ranganathan, P. *et al.* Preclinical activity of a novel CRM1 inhibitor in acute myeloid leukemia. *Blood* **120**, 1765-1773 (2012). https://doi.org/10.1182/blood-2012-04-423160

6 Zheng, Y. *et al.* KPT-330 inhibitor of XPO1-mediated nuclear export has anti-proliferative activity in hepatocellular carcinoma. *Cancer Chemother Pharmacol* **74**, 487-495 (2014). https://doi.org/10.1007/s00280-014-2495-8

7 Kwanten, B. *et al.* E3 ubiquitin ligase ASB8 promotes selinexor-induced proteasomal degradation of XPO1. *Biomed Pharmacother* **160**, 114305 (2023). https://doi.org/10.1016/j.biopha.2023.114305

8 Bondeson, D. P. & Crews, C. M. Targeted Protein Degradation by Small Molecules. *Annu Rev Pharmacol Toxicol* **57**, 107-123 (2017). https://doi.org/10.1146/annurev-pharmtox-010715-103507

9 Chamberlain, P. P. *et al.* Structure of the human Cereblon-DDB1-lenalidomide complex reveals basis for responsiveness to thalidomide analogs. *Nat Struct Mol Biol* **21**, 803-809 (2014). https://doi.org/10.1038/nsmb.2874

10 Bussiere, D. E. *et al.* Structural basis of indisulam-mediated RBM39 recruitment to DCAF15 E3 ligase complex. *Nat Chem Biol* **16**, 15-23 (2020). https://doi.org/10.1038/s41589-019-0411-6

11 Komiyama, K. *et al.* Antitumor activity of leptomycin B. *J Antibiot (Tokyo)* **38**, 427-429 (1985).

12 Newlands, E. S., Rustin, G. J. & Brampton, M. H. Phase I trial of elactocin. *Br J Cancer* **74**, 648-649 (1996). https://doi.org/10.1038/bjc.1996.415

13 Parikh, K., Cang, S., Sekhri, A. & Liu, D. Selective inhibitors of nuclear export (SINE)--a novel class of anti-cancer agents. *J Hematol Oncol* **7**, 78 (2014). https://doi.org/10.1186/s13045-014-0078-0

14 Attiyeh, E. F. *et al.* Pharmacodynamic and genomic markers associated with response to the XPO1/CRM1 inhibitor selinexor (KPT-330): A report from the pediatric preclinical testing program. *Pediatr Blood Cancer* **63**, 276-286 (2016). https://doi.org/10.1002/pbc.25727

15 Etchin, J. *et al.* Activity of a selective inhibitor of nuclear export, selinexor (KPT-330), against AML-initiating cells engrafted into immunosuppressed NSG mice. *Leukemia* **30**, 190-199 (2016). https://doi.org/10.1038/leu.2015.194

16 Yoshimura, M. *et al.* Induction of p53-mediated transcription and apoptosis by exportin-1 (XPO1) inhibition in mantle cell lymphoma. *Cancer Sci* **105**, 795-801 (2014). https://doi.org/10.1111/cas.12430

17 Hing, Z. A. *et al.* Next-generation XPO1 inhibitor shows improved efficacy and in vivo tolerability in hematological malignancies. *Leukemia* **30**, 2364-2372 (2016). https://doi.org/10.1038/leu.2016.136
18 Syed, Y. Y. Selinexor: First Global Approval. *Drugs* **79**, 1485-1494 (2019). https://doi.org/10.1007/s40265-019-01188-9
19 Vercruysse, T. *et al.* The Second-Generation Exportin-1 Inhibitor KPT-8602 Demonstrates Potent Activity against Acute Lymphoblastic Leukemia. *Clin Cancer Res* **23**, 2528-2541 (2017). https://doi.org/10.1158/1078-0432.CCR-16-1580
20 Daelemans, D. *et al.* A synthetic HIV-1 Rev inhibitor interfering with the CRM1-mediated nuclear export. *Proc Natl Acad Sci U S A* **99**, 14440-14445 (2002). https://doi.org/10.1073/pnas.212285299
21 Abdul Razak, A. R. *et al.* First-in-Class, First-in-Human Phase I Study of Selinexor, a Selective Inhibitor of Nuclear Export, in Patients With Advanced Solid Tumors. *J Clin Oncol* **34**, 4142-4150 (2016). https://doi.org/10.1200/JCO.2015.65.3949
22 Van Neck, T. *et al.* Inhibition of the CRM1-mediated nucleocytoplasmic transport by N-azolylacrylates: structure-activity relationship and mechanism of action. *Bioorg Med Chem* **16**, 9487-9497 (2008). https://doi.org/10.1016/j.bmc.2008.09.051
23 Lapalombella, R. *et al.* Selective inhibitors of nuclear export show that CRM1/XPO1 is a target in chronic lymphocytic leukemia. *Blood* **120**, 4621-4634 (2012). https://doi.org/10.1182/blood-2012-05-429506
24 Sun, Q. *et al.* Nuclear export inhibition through covalent conjugation and hydrolysis of Leptomycin B by CRM1. *Proc Natl Acad Sci U S A* **110**, 1303-1308 (2013). https://doi.org/10.1073/pnas.1217203110
25 Etchin, J. *et al.* Antileukemic activity of nuclear export inhibitors that spare normal hematopoietic cells. *Leukemia* **27**, 66-74 (2013). https://doi.org/10.1038/leu.2012.219
26 Haines, J. D. *et al.* Nuclear export inhibitors avert progression in preclinical models of inflammatory demyelination. *Nat Neurosci* **18**, 511-520 (2015). https://doi.org/10.1038/nn.3953
27 Walker, J. S. *et al.* Recurrent XPO1 mutations alter pathogenesis of chronic lymphocytic leukemia. *J Hematol Oncol* **14**, 17 (2021). https://doi.org/10.1186/s13045-021-01032-2
28 Neggers, J. E. *et al.* Identifying drug-target selectivity of small-molecule CRM1/XPO1 inhibitors by CRISPR/Cas9 genome editing. *Chem Biol* **22**, 107-116 (2015). https://doi.org/10.1016/j.chembiol.2014.11.015
29 Sakakibara, K. *et al.* CBS9106 is a novel reversible oral CRM1 inhibitor with CRM1 degrading activity. *Blood* **118**, 3922-3931 (2011). https://doi.org/10.1182/blood-2011-01-333138
30 Saito, N. *et al.* CBS9106-induced CRM1 degradation is mediated by cullin ring ligase activity and the neddylation pathway. *Mol Cancer Ther* **13**, 3013-3023 (2014). https://doi.org/10.1158/1535-7163.MCT-14-0064

31 Mendonca, J. *et al.* Selective inhibitors of nuclear export (SINE) as novel therapeutics for prostate cancer. *Oncotarget* **5**, 6102-6112 (2014). https://doi.org/10.18632/oncotarget.2174
32 Azmi, A. S. *et al.* Targeting the Nuclear Export Protein XPO1/CRM1 Reverses Epithelial to Mesenchymal Transition. *Sci Rep* **5**, 16077 (2015). https://doi.org/10.1038/srep16077
33 Wang, S., Han, X., Wang, J., Yao, J. & Shi, Y. Antitumor effects of a novel chromosome region maintenance 1 (CRM1) inhibitor on non-small cell lung cancer cells in vitro and in mouse tumor xenografts. *PLoS One* **9**, e89848 (2014). https://doi.org/10.1371/journal.pone.0089848
34 Kudo, N. *et al.* Leptomycin B inactivates CRM1/exportin 1 by covalent modification at a cysteine residue in the central conserved region. *Proc Natl Acad Sci U S A* **96**, 9112-9117 (1999). https://doi.org/10.1073/pnas.96.16.9112
35 Liu, Y. *et al.* Molecular cloning and characterization of the human ASB-8 gene encoding a novel member of ankyrin repeat and SOCS box containing protein family. *Biochem Biophys Res Commun* **300**, 972-979 (2003). https://doi.org/10.1016/s0006-291x(02)02971-6
36 Lumpkin, R. J., Baker, R. W., Leschziner, A. E. & Komives, E. A. Structure and dynamics of the ASB9 CUL-RING E3 Ligase. *Nat Commun* **11**, 2866 (2020). https://doi.org/10.1038/s41467-020-16499-9
37 Kohroki, J., Nishiyama, T., Nakamura, T. & Masuho, Y. ASB proteins interact with Cullin5 and Rbx2 to form E3 ubiquitin ligase complexes. *FEBS Lett* **579**, 6796-6802 (2005). https://doi.org/10.1016/j.febslet.2005.11.016
38 Mahrour, N. *et al.* Characterization of Cullin-box sequences that direct recruitment of Cul2-Rbx1 and Cul5-Rbx2 modules to Elongin BC-based ubiquitin ligases. *J Biol Chem* **283**, 8005-8013 (2008). https://doi.org/10.1074/jbc.M706987200
39 Saito, N. & Matsuura, Y. A 2.1-A-resolution crystal structure of unliganded CRM1 reveals the mechanism of autoinhibition. *J Mol Biol* **425**, 350-364 (2013). https://doi.org/10.1016/j.jmb.2012.11.014
40 Monecke, T. *et al.* Structural basis for cooperativity of CRM1 export complex formation. *Proc Natl Acad Sci U S A* **110**, 960-965 (2013). https://doi.org/10.1073/pnas.1215214110
41 Koyama, M. & Matsuura, Y. An allosteric mechanism to displace nuclear export cargo from CRM1 and RanGTP by RanBP1. *EMBO J* **29**, 2002-2013 (2010). https://doi.org/10.1038/emboj.2010.89
42 Kim, Y. K. *et al.* Structural basis of intersubunit recognition in elongin BC-cullin 5-SOCS box ubiquitin-protein ligase complexes. *Acta Crystallogr D Biol Crystallogr* **69**, 1587-1597 (2013). https://doi.org/10.1107/S0907444913011220
43 Kostrhon, S. *et al.* CUL5-ARIH2 E3-E3 ubiquitin ligase structure reveals cullin-specific NEDD8 activation. *Nat Chem Biol* **17**, 1075-1083 (2021). https://doi.org/10.1038/s41589-021-00858-8
44 Duda, D. M. *et al.* Structural insights into NEDD8 activation of cullin-RING ligases: conformational control of conjugation. *Cell* **134**, 995-1006 (2008). https://doi.org/10.1016/j.cell.2008.07.022

45 Jardin, F. *et al.* Recurrent mutations of the exportin 1 gene (XPO1) and their impact on selective inhibitor of nuclear export compounds sensitivity in primary mediastinal B-cell lymphoma. *Am J Hematol* **91**, 923-930 (2016). https://doi.org/10.1002/ajh.24451
46 Xie, Q. L., Liu, Y. & Zhu, Y. Chromosome region maintenance 1 expression and its association with clinical pathological features in primary carcinoma of the liver. *Exp Ther Med* **12**, 59-68 (2016). https://doi.org/10.3892/etm.2016.3283
47 Hing, Z. A. *et al.* Exploring the Role of the Recurrent Exportin 1 (XPO1/CRM1) Mutations E571G and E571K in Chronic Lymphocytic Leukemia. *Blood* **128**, 972-972 (2016). https://doi.org/10.1182/blood.V128.22.972.972
48 Navarro-Bailon, A. *et al.* Exportin-1 E571K mutation is a common finding in patients with classical Hodgkin lymphoma. *Hematol Oncol* **37**, 215-218 (2019). https://doi.org/10.1002/hon.2570
49 Dong, X. *et al.* Structural basis for leucine-rich nuclear export signal recognition by CRM1. *Nature* **458**, 1136-1141 (2009). https://doi.org/10.1038/nature07975
50 Port, S. A. *et al.* Structural and Functional Characterization of CRM1-Nup214 Interactions Reveals Multiple FG-Binding Sites Involved in Nuclear Export. *Cell Rep* **13**, 690-702 (2015). https://doi.org/10.1016/j.celrep.2015.09.042
51 Koyama, M., Shirai, N. & Matsuura, Y. Structural insights into how Yrb2p accelerates the assembly of the Xpo1p nuclear export complex. *Cell Rep* **9**, 983-995 (2014). https://doi.org/10.1016/j.celrep.2014.09.052
52 Fung, H. Y., Fu, S. C., Brautigam, C. A. & Chook, Y. M. Structural determinants of nuclear export signal orientation in binding to exportin CRM1. *Elife* **4** (2015). https://doi.org/10.7554/eLife.10034
53 Fung, H. Y., Fu, S. C. & Chook, Y. M. Nuclear export receptor CRM1 recognizes diverse conformations in nuclear export signals. *Elife* **6** (2017). https://doi.org/10.7554/eLife.23961
54 Cao, S. *et al.* Defining molecular glues with a dual-nanobody cannabidiol sensor. *Nat Commun* **13**, 815 (2022). https://doi.org/10.1038/s41467-022-28507-1
55 Lei, Y. *et al.* Structure-Guided Design of the First Noncovalent Small-Molecule Inhibitor of CRM1. *J Med Chem* **64**, 6596-6607 (2021). https://doi.org/10.1021/acs.jmedchem.0c01675
56 Skaar, J. R., Pagan, J. K. & Pagano, M. Mechanisms and function of substrate recruitment by F-box proteins. *Nat Rev Mol Cell Biol* **14**, 369-381 (2013). https://doi.org/10.1038/nrm3582
57 Sheard, L. B. *et al.* Jasmonate perception by inositol-phosphate-potentiated COI1-JAZ co-receptor. *Nature* **468**, 400-405 (2010). https://doi.org/10.1038/nature09430
58 Tan, X. *et al.* Mechanism of auxin perception by the TIR1 ubiquitin ligase. *Nature* **446**, 640-645 (2007). https://doi.org/10.1038/nature05731
59 Ito, T. *et al.* Identification of a primary target of thalidomide teratogenicity. *Science* **327**, 1345-1350 (2010). https://doi.org/10.1126/science.1177319
60 Fischer, E. S. *et al.* Structure of the DDB1-CRBN E3 ubiquitin ligase in complex with thalidomide. *Nature* **512**, 49-53 (2014). https://doi.org/10.1038/nature13527

61 Du, X. *et al.* Structural Basis and Kinetic Pathway of RBM39 Recruitment to DCAF15 by a Sulfonamide Molecular Glue E7820. *Structure* **27**, 1625-1633 e1623 (2019). https://doi.org/10.1016/j.str.2019.10.005
62 Slabicki, M. *et al.* The CDK inhibitor CR8 acts as a molecular glue degrader that depletes cyclin K. *Nature* **585**, 293-297 (2020). https://doi.org/10.1038/s41586-020-2374-x
63 Slabicki, M. *et al.* Small-molecule-induced polymerization triggers degradation of BCL6. *Nature* **588**, 164-168 (2020). https://doi.org/10.1038/s41586-020-2925-1
64 Wu, Y. L. *et al.* Structural basis for an unexpected mode of SERM-mediated ER antagonism. *Mol Cell* **18**, 413-424 (2005). https://doi.org/10.1016/j.molcel.2005.04.014
65 Schneider, C. A., Rasband, W. S. & Eliceiri, K. W. NIH Image to ImageJ: 25 years of image analysis. *Nat Methods* **9**, 671-675 (2012). https://doi.org/10.1038/nmeth.2089
66 Fung, H. Y. J. & Chook, Y. M. Binding Affinity Measurement of Nuclear Export Signal Peptides to Their Exporter CRM1. *Methods Mol Biol* **2502**, 245-256 (2022). https://doi.org/10.1007/978-1-0716-2337-4_16
67 Mastronarde, D. N. Automated electron microscope tomography using robust prediction of specimen movements. *J Struct Biol* **152**, 36-51 (2005). https://doi.org/10.1016/j.jsb.2005.07.007
68 Punjani, A., Rubinstein, J. L., Fleet, D. J. & Brubaker, M. A. cryoSPARC: algorithms for rapid unsupervised cryo-EM structure determination. *Nat Methods* **14**, 290-+ (2017). https://doi.org/10.1038/Nmeth.4169
69 Bepler, T. *et al.* Positive-unlabeled convolutional neural networks for particle picking in cryo-electron micrographs. *Nat Methods* **16**, 1153-1160 (2019). https://doi.org/10.1038/s41592-019-0575-8
70 Pettersen, E. F. *et al.* UCSF chimera - A visualization system for exploratory research and analysis. *J Comput Chem* **25**, 1605-1612 (2004). https://doi.org/10.1002/jcc.20084
71 Pettersen, E. F. *et al.* UCSF ChimeraX: Structure visualization for researchers, educators, and developers. *Protein Sci* **30**, 70-82 (2021). https://doi.org/10.1002/pro.3943
72 Adams, P. D. *et al.* PHENIX: a comprehensive Python-based system for macromolecular structure solution. *Acta Crystallogr D* **66**, 213-221 (2010). https://doi.org/10.1107/S0907444909052925
73 Croll, T. I. ISOLDE: a physically realistic environment for model building into low-resolution electron-density maps. *Acta Crystallogr D Struct Biol* **74**, 519-530 (2018). https://doi.org/10.1107/S2059798318002425
74 Emsley, P. New Tools for Ligand Refinement and Validation in Coot and CCP4. *Acta Crystallogr A* **74**, A390-A390 (2018). https://doi.org/10.1107/S0108767318096101
75 Sanchez-Garcia, R. *et al.* DeepEMhancer: a deep learning solution for cryo-EM volume post-processing. *Commun Biol* **4**, 874 (2021). https://doi.org/10.1038/s42003-021-02399-1
76 Schrodinger, LLC. *The PyMOL Molecular Graphics System, Version 2.4* (2020).

77 Krissinel, E. & Henrick, K. Inference of macromolecular assemblies from crystalline state. *J Mol Biol* **372**, 774-797 (2007). https://doi.org/10.1016/j.jmb.2007.05.022
78 Jurrus, E. *et al.* Improvements to the APBS biomolecular solvation software suite. *Protein Sci* **27**, 112-128 (2018). https://doi.org/10.1002/pro.3280
79 Fung, H. Y. J. & Chook, Y. M. Crystallization of Nuclear Export Signals or Small-Molecule Inhibitors Bound to Nuclear Exporter CRM1. *Methods Mol Biol* **2502**, 285-297 (2022). https://doi.org/10.1007/978-1-0716-2337-4_19
80 Minor, W., Cymborowski, M., Otwinowski, Z. & Chruszcz, M. HKL-3000: the integration of data reduction and structure solution--from diffraction images to an initial model in minutes. *Acta Crystallogr D Biol Crystallogr* **62**, 859-866 (2006). https://doi.org/10.1107/S0907444906019949
81 Moriarty, N. W., Grosse-Kunstleve, R. W. & Adams, P. D. electronic Ligand Builder and Optimization Workbench (eLBOW): a tool for ligand coordinate and restraint generation. *Acta crystallographica. Section D, Biological crystallography* **65**, 1074-1080 (2009). https://doi.org/10.1107/S0907444909029436
82 Afonine, P. V. *et al.* Towards automated crystallographic structure refinement with phenix.refine. *Acta crystallographica. Section D, Biological crystallography* **68**, 352-367 (2012). https://doi.org/10.1107/S0907444912001308
83 Emsley, P., Lohkamp, B., Scott, W. G. & Cowtan, K. Features and development of Coot. *Acta crystallographica. Section D, Biological crystallography* **66**, 486-501 (2010). https://doi.org/10.1107/S0907444910007493